Physics – Uspekhi **66** (8) 794 – 817 (2023)

REVIEWS OF TOPICAL PROBLEMS PACS numbers: 42.30.Ms, 42.30.Va, 42.30.Wb, 42.62.Be, 62.20.D–, 62.20.F–

Optical coherence tomography in elastography and angiography [1]

V Yu Zaitsev

DOI: https://doi.org/10.3367/UFNe.2022.06.039207

Contents

1. Introduction **794**
2. Basic principles of optical coherence tomography imaging **796**
3. Principles of optical coherence tomography angiography and examples of its use **799**
3.1 Doppler approach; 3.2 Correlation approach in optical coherence tomography angiography; 3.3 Angiography based on temporal variability of speckle intensity in optical coherence tomography; 3.4 Method using high-pass filtering to extract the signal variability in vessels
4. Principles of optical coherence elastography and examples of its use **804**
4.1 Optical coherence elastography based on measuring the velocities of shear and surface waves; 4.2 Compression optical coherence elastography and strain visualization in optical coherence tomography; 4.3 Correlation approach in optical coherence tomography; 4.4 Phase approach to visualization of displacements and strains in optical coherence tomography; 4.5 Experimental examples of strain imaging in optical coherence tomography by the vector method; 4.6 Quantification of stress–strain curves and Young's modulus of biotissues; 4.7 Quantitative elastospectroscopy based on compression optical coherence elastography for optical biopsy and determination of tumor margins for resection
5. Conclusion **816**
References **816**

Abstract. An overview of modalities that are new for biomedical diagnostics and that have emerged in recent years in optical coherence tomography (OCT) — optical coherence tomography angiography (OCTA) and optical coherence elastography (OCE) — is given. These modalities are extensions of OCT imaging technology, which is based on the principles of low-coherence interferometry and celebrated its 30th anniversary in 2021. The basic principles of OCTA and OCE are outlined, the appearance of which was largely stimulated by earlier similar functional extensions in medical ultrasound. A number of results are presented that illustrate previously inaccessible possibilities opened up by the new modalities for biomedical applications. The article is an extended version of the report presented at the Scientific Session of the Division of Physical Sciences of the Russian Academy of Sciences, held on December 13, 2021.

Keywords: optical coherence tomography, optical coherence tomography angiography, optical coherence elastography, compression elastography, biophotonics, optical biopsy

1. Introduction

Optical coherence tomography (OCT) is a rapidly growing technology of optical imaging, primarily for biomedical applications. In comparison with medical imaging methods, already widely used in clinics, such as medical ultrasound investigation (USI) and magnetic resonance imaging (MRI) (having emerged in the 1940s and 1950s, respectively), OCT is a much younger technology. The history of OCT is traditionally associated with paper [1] of 1991, in which the very term 'optical coherence tomography' was introduced and the images of an eye retina obtained using it were demonstrated. Review [2] published in 2021 resumes the OCT development of over three decades: more than 75,000 papers have been published and several dozen companies have been involved in OCT commercialization with the prospect for a global market of $\sim$ 1.5 billion dollars by 2023. Moreover, OCT technologies can be considered among the most rapidly introduced imaging methods and have already demonstrated substantial clinically, socially, and economically significant results.

From the viewpoint of imaging resolution and depth, OCT fills the gap between optical microscopy and medical ultrasound widely used in the clinic. The diagram in Fig. 1 illustrates a comparison of scales and resolution of various imaging technologies. For OCT, the typical resolution is seen to be about 5–15 micrometers (although there are OCT devices with higher resolution). The OCT imaging depth is usually restricted to a value of 1–2 mm, determined by the scattering of the optical beam and its attenuation in strongly scattering biotissues. Therefore, it is attempted to choose the working wavelength in biotissue transparency windows, often using near infrared (IR) radiation, e.g., with a wavelength of 1.3 μm.

V Yu Zaitsev. A V Gaponov-Grekhov Institute of Applied Physics, Russian Academy of Sciences,
ul. Ulyanova 46, 603950 Nizhny Novgorod, Russian Federation
E-mail: vyuzai@ipfran.ru

Received 11 April 2022, revised 14 June 2022
Uspekhi Fizicheskikh Nauk **193** (8) 845 – 871 (2023)
Translated by V L Derbov

[1] The present review is an extended version of the report presented at the Scientific Session of the Division of Physical Sciences of the Russian Academy of Sciences (RAS), held on December 13, 2021.

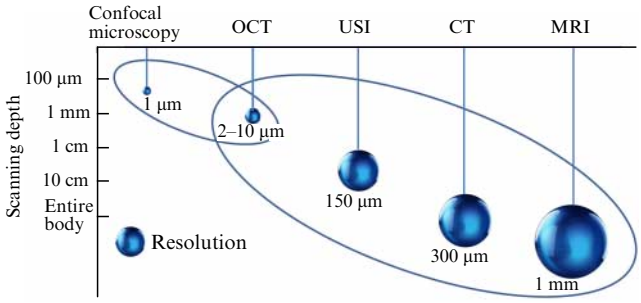

Figure 1. Comparison of scales of regions of visualization and resolution for various technologies of biomedical imaging. CT — Computer Tomography.

In spite of a relatively small imaging depth, there is a wide field of biomedical applications where such an imaging depth is quite sufficient, and the OCT resolution, which is much higher than that of USI and MRI, plays the key role. Above all, this concerns ophthalmological applications, where OCT enables not only examining the cornea and lens in detail but also exploring the bottom of the eye to the entire depth of the retina, providing a fairly wide field of view in lateral directions. Therefore, it is no coincidence that OCT very much revolutionized exactly ophthalmology diagnostics and therapy monitoring. As noted in Ref. [2], an OCT scan of a patient's retina is performed every second in the world. In the history of ophthalmology, OCT has become the fastest-growing imaging technology in clinical practice, far surpassing the former 'gold standard' of ultrasound-based ophthalmic imaging. This is largely because, in terms of the informativeness of retina investigation, OCT approached another 'gold standard,' the histological study of biotissues that essentially requires biopsy sampling, which in the case of the retina is impossible.

Note also that combining with such instruments as endoscopes, catheters, or various needle or flexible intravascular probes opens up for OCT possibilities that largely overcome the imaging depth limitations. Moreover, the typical dimensions of the OCT imaging region (about 4–8 mm laterally and 1–2 mm in depth) are quite comparable with the dimensions of the studied biopsy samples. In this regard, from the very beginning of OCT, much attention was paid to the study of the possibilities opened up by OCT for performing optical biopsies based on the analysis of OCT data in order to make their informativeness closer to that of standard histologic investigations. Another expected advantage of OCT, along with an informativeness comparable to that of histology, could be the possibility of exploring directly fresh-extracted samples or even *in vivo* tissue (at accessible localizations). It is important to recall here that preparation of a standard histological specimen takes several days and includes chemical fixation of a tissue sample, dehydration, paraffinizing thin sectioning, and staining with special dyes. Besides, the analysis of histologic specimens requires the participation of a qualified histopathologist and is hard for automation. One of the most important goals of histological investigations is the diagnostics of oncologic diseases with the most reliable differentiation of malignant neoplasms from still benign neoplasms and normal tissue. The demand for such diagnostics is high for intraoperative use in particular, in breast cancer surgery, when it is of primary importance to control clean tumor resection margins in order to exclude a recurrence. Ideally, such a control should be performed during the operation, nearly in real time (in a few minutes), which requires innovative solutions, since the traditional 'gold standard' histologic procedures do not enable it.

In this regard, the advent of OCT has given rise to great hopes that, based on the analysis of OCT scans, it will be possible to reliably differentiate between malignant and benign tissues. This problem of paramount importance has stimulated a large number of studies aimed at finding the corresponding differences, first using conventional structural OCT images and then polarization-sensitive ones (e.g., obtained by comparing scans with the original polarization and the orthogonal one [3]). In addition, as for ultrasound images, there has been natural interest in using differences in 'echogenicity' (i.e., signal magnitude) from different scattering areas or differences in depth attenuation of the OCT signal (attenuation imaging). Although initial hopes have still not been realized completely, beginning in the 1990s, a number of promising results were obtained, confirming that even though OCT scans enable no cell resolution, it can be possible to find in the OCT images some macroscopic informative signs caused by subresolution microstructure features, which can be used for tissue differentiation. In addition, since OCT images have a characteristic speckle structure due to the interference of fields from sub-resolution scatterers, it is of great interest to study the characteristics of OCT speckles that reflect the features of the unresolved microstructure. These studies include clarifying physical mechanisms of the OCT speckle formation, e.g., [4–6], and empirical searching for differences among the statistical characteristics of OCT speckles in various tissues [7, 8]. This field, often referred to as texture analysis, is still under active development, and in recent years multifactor approaches using neural networks and machine learning have begun to be widely used; for example, Refs [9–11] describe such approaches to the differentiation of tumor and nontumor tissues (see also collective monographs [12, 13] and references therein).

Thus, one of the most rapidly progressing OCT trends is the development of OCT functional extensions, also referred to as novel OCT modalities. In this regard, an important stimulating role belongs to analogies between OCT and ultrasonic studies, where such functional extensions began to develop much earlier. This relates, above all, to such USI modalities as elastography (i.e., visualization of local strains and elastic properties of biotissues) and angiography (visualization of blood circulation) [14–16]. In the context of comparison with USI, it looks symbolic that, in the same year 1991 when paper [1] was published, starting the rapid OCT progress, paper [17] was also published, which stimulated subsequent explosive development of elastography, not only in USI but also in a number of methods of medical imaging.

Since, in spite of all the differences among imaging methods and characteristic scales, there is an obvious similarity between USI images and OCT scans, so that it seems quite natural that, with the advance of OCT, the ideas of developing its new modalities emerged by analogy with USI. In this connection, the paper by Schmidt [18] published in 1998 became an important milestone, where it was proposed to create an elastographic OCT modality by analogy with USI. However, whereas after a decade of preliminary studies ultrasound elastography began active clinical use already in the early 2000s and was implemented on several USI scanner platforms, in OCT, attempts at direct transfer of elastographic principles from USI were not

sufficiently efficient, and a substantial advance in OCT elastography was achieved only in the last 5–7 years. A little earlier, similar advances occurred in OCT angiography. However, in spite of the already apparent success in developing these modalities, OCT angiography was offered only in ophthalmological OCT instruments (presently dominating among OCT devices clinically used). There are still no mass-produced OCT scanners with an elastography function on the world market, although a breakthrough toward their wide practical application should obviously occur in the coming years.

In the thorough review [2] of the 30 years of the OCT development history mentioned above, based on the analysis of almost 400 publications, it is concluded that the development and clinical introduction of multimodal OCT (including the elastographic and angiographic modalities) is exactly what is expected to become one of the main OCT development trends in the next decade. Of course, for wide use of the new OCT modalities, it is also very important to further improve engineering and physical solutions for obtaining initial OCT scans, a discussion of which can also be found in [2].

The main goal of the present review is to discuss recent advances in the development of OCT angiography and, mainly, OCT elastography, with a significant emphasis on the most promising results recently obtained in Russia based on original physical approaches, which are of great interest for a wide range of biomedical applications.

Section 2 briefly discusses the main principles of obtaining initial OCT images. Section 3 considers the principles of implementing OCT angiography and presents some examples of its use for biomedical problems not related to the visualization of blood flow in the fundus of the eye, which is the most frequently discussed application of OCT angiography (see, e.g., [19]). The main focus in Section 4 is or approaches proposed for implementing OCT elastography, with the emphasis on the original version of quantitative elastography of the so-called compression type, developed in Russia. The discussion of this approach is insufficiently presented in the most reviews that have appeared in recent years. We present examples of using OCT elastography as a base for implementing some kind of 'elastospectroscopy' (by analogy with the notion of 'mass spectroscopy' also used in biomedical studies [20, 21]) that enables highly selective multicomponent segmentation of histological components of biotissues, the results of which turn out to be very close to those of standard histological examinations.

2. Basic principles of optical coherence tomography imaging

OCT imaging is based on the principles of low-coherence interferometry, the implementation of which during the existence of OCT has somewhat evolved. Although OCT tomographs do not directly use short light pulses, in a broader sense it is possible to notice some analogy with the echo pulsed principle of imaging in ultrasonic scanners. This analogy is particularly clear in the so-called time-domain OCT using the time delay to enable depth resolution. However, instead of real femtosecond optical pulses, time-domain OCT uses effective 'correlation pulses' having the appropriate short duration. Such effective pulses can be formed by correlation processing of broadband optical-noise signals from diode sources with a small enough coherence length. For this purpose, to selectively acquire a signal backscattered from a certain depth of the studied region, a Michelson interferometer is used. The light beam from the source is divided into two arms, the reference arm and the signal one (Fig. 2a). In the signal arm, the optical radiation usually is weakly focused to obtain a beam of nearly constant diameter over the entire imaging depth of 1–2 mm. The beam can be scanned in the lateral direction, the lateral resolution being determined by the beam radius. The received signal backscattered from the medium is mixed with the signal from the reference arm and arrives at a photodetector. Both signals are multiplied and time integrated at the detector nonlinearity, i.e., the operation of their cross correlation is executed. Before merging with the signal beam, the optical signal in the reference arm is reflected from a moving mirror, so that the mutual coherence (and the nonzero amplitude of the effective correlation pulse) takes place only upon coincidence of the optical path lengths of the two beams mixed at the photodetector. As a result, the correlation pulse recorded at the fixed position of the reference mirror turns out to be proportional to the amplitude of the signal scattered from exactly the depth for which equality of the optical path lengths in the reference and signal arms takes place. The spatial length of such a correlation pulse depends on the coherence length of the source field and determines the depth resolution. The modulation of the reference arm length

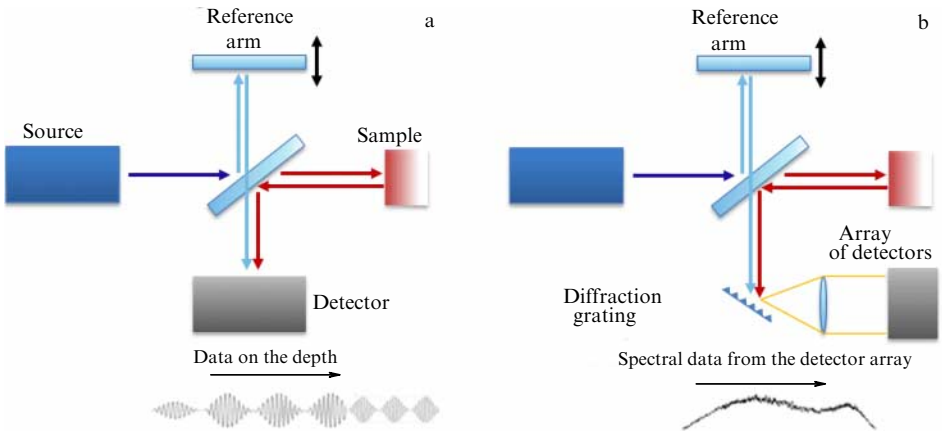

Figure 2. Illustration of the principle of OCT image formation based on signal processing in time (a) and spectral (b) domains.

enables depth scanning. To ensure a sufficient imaging depth, the modulation amplitude of the reference arm length should be sufficiently large (several millimeters).

The above principle of OCT imaging dominated for 10–15 years. Its main drawback was the limited scanning rate (a few kilohertz) that determines the rate of recording one-dimensional depth scans (A-scans). Since several hundred or thousands of A-scans are required to form a 2D or 3D image, this limits the acquisition rate of even 2D scans to a few hertz, which is many times slower than the acquisition rate of ultrasound scans.

An alternative to the high-amplitude modulation of the reference arm providing depth scanning has been found; it is based on an essentially different approach to the formation of OCT images, referred to as spectral-domain OCT (SD OCT). At present, most OCT instruments use this spectral principle, which is illustrated in Fig. 2b. As is seen from Fig. 2b, the interference signal first arrives at a dispersion element. Then, the spectral components with different wave numbers propagate at different angles, which allows simultaneous recording of each of the components separately by an array of a few hundred or thousands of photodetectors.

As a result of nonlinear mixing of the reference and signal waves at each nth photodetector with averaging-off fast-varying components at optical frequencies, it is possible to eliminate the DC components, determined by the intensities of the reference and signal waves. Only the contribution from cross terms with the form $A_\mathrm{r}A_\mathrm{s}\exp(\mathrm{i}k_n\Delta z)$, where A_s and A_r are amplitudes of the signal and reference waves, are left. Without loss of generality, the reference wave amplitude A_r can be assumed to be equal to unity. The quantity $k_n\Delta z$ corresponds to the difference in phase incursions due to the difference in optical path lengths between the reference wave and the signal one (i.e., the phase incursion in the reference arm is taken as the origin for measuring the signal wave phase).

Hence, the signal amplitudes having the form $A_\mathrm{s}\exp(\mathrm{i}k_nz)$, recorded by individual photodetectors, are, in fact, complex amplitudes of the spatial Fourier components of the signal field with the corresponding wave numbers. Due to its narrow band, each individual component of the signal field has a large coherence length, overlying the entire depth to be imaged. Therefore, the field of each spectral component is determined by the contributions of all scatterers from different depths in the probing beam, so that the received signal at each spatial frequency k_n does not yet enable depth resolution. However, if the amplitudes of all spectral components in the array of detectors are known, then the inverse Fourier transform already gives a spatially resolved image corresponding to the distribution of the backscattered signal amplitudes within the imaged depth. Therefore, in general, the relationship between the recorded spectral amplitudes and the constructed spatial depth distribution, with some caveats, is similar to the relationship between spectral and spatial data for the conventional forward and inverse Fourier transforms.

Notably, by analogy with the discrete Fourier transform, the finite step $\delta k = |k_{n+1} - k_n|$ between the wave numbers of adjacent Fourier components $\exp(\pm\mathrm{i}k_nz)$ (where z is the spatial coordinate along which the probing field propagates) leads to the finite size $z = H$ of the region of unambiguous visualization. Outside this region, the image will periodically repeat. In the case of the usual mathematical Fourier transform, the periodicity is determined by the known condition $H = 2\pi/\delta k$. However, in the discussed case of the image obtained in spectral OCT, the region of periodicity is half the size, $H = \pi/\delta k$, due to the twofold phase accumulation by the probing wave that passes first into the depth of the medium and then back to the receiver [22–24]. It is important to emphasize that such values can be obtained if the receivers measure both quadratures (sine and cosine) of the complex spectral harmonic $\exp(\pm\mathrm{i}k_nz)$. However, from Fig. 2b, illustrating the spectral principle of OCT imaging, it is clear that, for the fixed length of the reference arm, only one quadrature component can be obtained. To get both quadratures, as in radiotechnical devices, it is necessary to use two reference signals, the phases of which are in quadrature. Practically, both quadratures can be obtained by quarter-wave modulation of the reference arm or, alternatively, by using two reference arms simultaneously. However, since the double-arm scheme substantially complicates the construction and increases the cost, a single-arm scheme is often used, as shown in Fig. 2b and, if necessary, the Hilbert transform is applied to present the single-quadrature signal $\cos(\mathrm{i}k_nz)$ as a double-quadrature one, $\exp(\mathrm{i}k_nz)$. At the same time, however, an additional ambiguity of phase changes appears (up to the sign), which leads to the fact that the maximum imaging depth $H = \pi/\delta k$ provided by a two-quadrature signal decreases again by a factor of two, i.e., to $H = \pi/(2\delta k)$ [22, 23]. As for the spatial resolution of the reconstructed image, in accordance with the properties of the Fourier transform, it is determined by the total width of the spectrum Δk of the probing signal, which physically determines its coherence length $L_\mathrm{c} \sim \pi/\Delta k \sim \lambda^2/(2\Delta\lambda)$, (where λ is the optical wavelength). For OCT systems, this resolution in structural images is 5–10 μm; moreover, as explained in Section 4, it is improper to transfer directly such resolution values to elastographic images, for which it is usually several times lower.

Note also that the simultaneous reception of many spectral components is not a unique way to implement the spectral principle of OCT imaging. Alternatively, the amplitudes of individual components of the received signal can be recorded sequentially in time using a frequency-tunable laser source whose tuning range width will play the same role as the total spectrum width of a low-coherence source. Although tunable sources are currently more expensive, only one photodetector instead of a large array need be used for reception. Therefore, this version of the implementation of spectral OCT has come to be used quite often [2].

As a final point of this introductory section, let us dwell on the possibility of measuring phase variations using broadband OCT devices to detect small (nanometer level) changes in the position of scatterers, which is of fundamental importance for further discussion. Usually, phase measurements are considered using highly coherent signals, whereas for OCT a radiation bandwidth of 5–10% is typical. At the same time, for Fourier transforms there is a relation (similar to the uncertainty relation between the coordinate and momentum in quantum mechanics) between the characteristic scales of data localization in the spectral and spatial domain: $\Delta k\Delta z_\mathrm{char} \sim \pi$, which determines the axial resolution of OCT images. In this connection, for the total number N of the recorded spectral components within the limits of the total depth of unambiguous visualization H discussed above, the same number N of spatial counts is obtained in the reconstructed image, i.e., it consists of pixels. Nevertheless, the discreteness of displaying the scatterer position does not negate the possibility of detecting changes in their axial position on scales, not only smaller than a pixel, but even

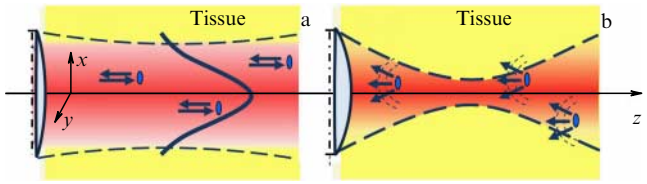

Figure 3. Illustration of modeling OCT signal formation within the approximation of discrete scatterers. (a) Approximation of weakly focused probing beam providing approximately the same depth resolution; in this case, it is possible to ignore the phase front curvature and divergence of the scattered signal from discrete scatterers, but to consider the beam amplitude profile according to simplified description [24]. (b) Accurate description of the amplitude-phase structure of the beam with its focusing, divergence of signals from scatterers taken into account, and accurate consideration of the scattered signal collection on the illumination/receiving aperture according to [26]. A comparison of these simplified and accurate descriptions in the case of a weakly focused beam is presented in Fig. 4. (Adapted from [26].)

significantly smaller than the mean optical wavelength, by variations in the phase of the incoming signal. In this case, the phases of individual pixels can be described practically in the same way as for a monochromatic signal, corresponding to the central wavelength of the OCT source.

For an explanation, it is possible to address a very simple model describing the complex amplitude of the qth pixel in a one-dimensional A-scan formed from N spectral components with the wave numbers k_n. When modeling OCT, the scattering medium is often presented as an ensemble of discrete subpixel scatterers [25]. In this case, even for such discrete (formally point-like) scatterers, it is easy to introduce various amplitudes of the scattered signal, imitating various dimensions of real small scatterers, to introduce a frequency dependence of the scattered signal, to attribute polarization-sensitive scattering, etc. Then, in correspondence with the very principle of constructing an 'ideal' image in OCT, a ballistic character of scattering is assumed, i.e., single scattering in the back direction, as shown schematically in Fig. 3 (whereas the scattering at other angles together with the absorption are included in the wave attenuation). In such a description of the main part of the OCT signal received by photodetectors, it is possible to ignore the substantially smaller-amplitude contribution of multiple scattering events to the backscattered signal, the components of which are additionally delayed relative to the main part of the singly scattered signal and can blur (in depth) the images of localized scatterers. Taking these notes into account, assuming that the scatterers localized in the beam have coordinates z_j, and omitting the factors responsible for the signal attenuation depending on the depth z, we can present the complex amplitude $A(q)$ for the qth pixel corresponding to the depth z_q in the form [24]

$$A(q) = \sum_j \sum_n S(k_n) A_j \exp\left(\mathrm{i}2k_n z_j\right) \exp\left(-\mathrm{i}\,\frac{2\pi n}{H}\,z_q\right)$$

$$= \sum_j \sum_n S(k_n) A_j \exp\left(\mathrm{i}2k_0 z_j\right)$$

$$\times \exp\left(\mathrm{i}\,\frac{2\pi n}{H}\,z_j\right) \exp\left(-\mathrm{i}\,\frac{2\pi n}{H}\,z_q\right). \qquad (1)$$

In expression (1), the contributions from the received spectral components are summed over the index n, and the contributions from all scatterers localized in the beam, over the index j. For the current discussion, it is sufficient to consider the spectrum shape $S(k_n)$ to be rectangular, as is the amplitude distribution in the beam cross section. Usually, these distributions are close to a Gaussian shape, and it is not difficult to consider them. The factor A_j corresponds to the signal amplitude from the jth scatterer. In expression (1) after the second equality sign, the central wavenumber is extracted from the set of wavenumbers k_n in the factor $\exp\left(\mathrm{i}2k_0 z_j\right)$, and the relation mentioned above between the maximal depth of unambiguous visualization and the step in wavenumber, $\delta k = k_{n+1} - k_n = \pi/H$, is taken into account. In spite of significant simplifications, in particular, omitting the geometric factors that describe the focusing of the beam itself and the spherical divergence of signals from localized scatterers, for the weakly focused beams used most often (providing nearly the same transverse resolution at different depths), this simple model enables a reasonable agreement with the substantially more sophisticated description (see, e.g., [26–28]), which accurately considers both the beam shape and the spherical divergence of fields from the localized scatterers.

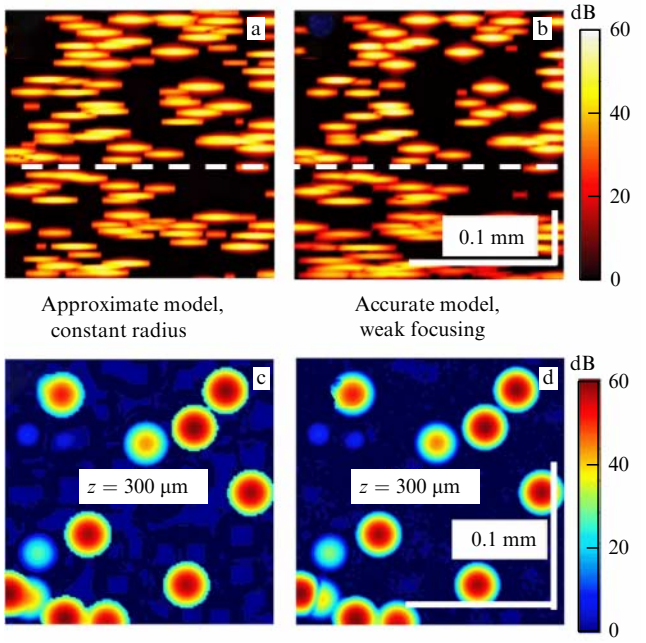

Figure 4. Comparison of results of modeling OCT scans for a weakly focused beam using the simplified (a, c) description [24, 29] that takes into account only the Gaussian amplitude profile and an accurate (b, d) description [26] of the Gaussian probe beam considering the divergence of the scattered fields from localized scatterers and the collection of the scattered signal on the receiving aperture. For clarity, a low concentration of scatterers is purposely chosen. Figures a and b show depth B-scans (in the xz-plane), figures c and d show scans corresponding to a top view from the side of the OCT probe (i.e., the horizontal en face scans in the xy-plane) for a depth of $z = 300$ μm, shown by a dashed line in the vertical B-scans in Figs a and b. (Adapted from [26], where color palettes of different types were used.)

Figure 4 shows an example of a comparison of the simulated cross sections in depth based on the simplified expression (1), supplemented only by taking into account the Gaussian amplitude profile of the beam [29], and based on a rigorous description of the amplitude-phase beam structure, the divergence of the scattered field, and its collection at the receiving aperture [26, 28]. As can be seen, rigorous consideration of the factors mentioned above leads to a very weak depth

dependence of the amplitudes of images of localized sources, yielding results close to those of the simplified description [24, 29] (Fig. 4b and d), very efficient for computations. These are exactly such weakly focused beams, providing nearly the same transverse resolution over the entire depth of a B-scan, which are used in most OCT systems. Vertical (along the z-axis) blurring of the images of point scatterers, as noted above, is determined by the coherence length of the probing field, whereas, in the horizontal direction, the image of a scatterer reproduces the transverse profile of the beam that performs scanning with an equal step of 4 μm along both horizontal coordinates, x and y (in the present example, the Gaussian beam radius is about 15 μm).

In the development of new modalities discussed below, numerical experiments using models [24, 26–28] have played a great role, allowing in ideally controllable numerical experiments a flexible variation of conditions and efficient testing of various new methods of OCT signal analysis, which could be much more difficult (and sometimes impossible) to reproduce in real physical experiments.

Let us discuss in more detail the phase of the pixel complex amplitude $A(q)$ in Eqn (1), assuming for simplicity that the spatial position of pixel z_q is close to the position z_j of a scatterer, localized within its limits, $z_q \approx z_j$. Obviously, upon the change of position of this scatterer by Δz_j, the change in the phase $\Delta\varphi(q)$ of this pixel is determined by the additional factors $\exp(\mathrm{i}2k_n\Delta z_j)$ in the sum over the spectral component index. For the fixed index j of a scatterer from the sum over the spectrum, the phase multiplier $\exp(\mathrm{i}2k_0\Delta z_j)$ is factored out. The residuary summed factors $\exp[\mathrm{i}2(k_n - k_0)\Delta z_j]$, provided that the spectrum shape is symmetric with respect to the centrum $k_n = k_0$, are complex conjugate terms, the summation of which yields real numbers that do not affect the phase. Therefore, when the scatterer is shifted by Δz_j, the phase change $\Delta\varphi(q)$ in the qth pixel is determined by the central factor $\exp(\mathrm{i}2k_0\Delta z_j)$, as for a monochromatic wave with the wave vector k_0:

$$\Delta\varphi(q) = 2k_0\Delta z_j = \frac{4\pi}{\lambda_0}\,\Delta z_j\,, \tag{2}$$

where $\lambda_0 = 2\pi/k_0$ is the central wavelength. Note that, in Eqns (1) and (2), the wavenumber corresponds to the field propagation through the biotissue, for which the values of the refractive index $n_\mathrm{t} \sim 1.3-1.4$ are typical; therefore, if the wavenumber in a vacuum is k_0^vac, then, in the tissue, $k_0 = n_\mathrm{t}k_0^\mathrm{vac}$. If the spectrum shape is not ideally symmetric, some phase corrections arise that shift the mean value of the wavenumber k_0 in Eqn (2), so that, as a result, only the proportionality coefficient between $\Delta\varphi(q)$ and Δz_j in Eqn (2) somewhat changes, which is not an obstacle to detecting $\Delta z_j \ll \lambda_0$. In practice, more significant errors are caused not by the systematic shift mentioned above but by the fact that the fields from neighboring scatterers in pixels that still fall within the coherence length (at least neighboring and even more distant pixels) leak into the considered pixel. For such scatterers, there can be a different shift value, which introduces random contributions to the phase shift for the given pixel $\Delta\varphi(q)$. Nevertheless, both real experiments and realistic modeling [27, 28] confirm that OCT enables measuring phase variations at a level of a few thousandths of the period (i.e., displacements of less than 1 nm), and that the simple interpretation of the pixel phase variation in accordance with Eqn (2) can be efficiently used to extract information about the motion of scatterers in the tissue.

Using such an analysis of the OCT signal variations, above all, the phase ones, caused by micromotions of subresolved scatterers, it turns out to be possible to construct such OCT extensions (or modalities) as microangiography and elastography. In Sections 3 and 4, these OCT modalities are discussed in more detail, with an emphasis on the results obtained in recent years by Russian researchers in the course of joint work between the Institute of Applied Physics of the Russian Academy of Sciences (IAP RAS) and biologists and physicians from the Privolzhsky Research Medical University (PRMU). A discussion of some other OCT extensions not related to selecting micromotions but also being beyond the framework of purely structural OCT imaging (e.g., using polarization effects) can be found in reviews [30, 31], where much attention is devoted to the state of these studies in Russia.

3. Principles of optical coherence tomography angiography and examples of its use

Interest in visualization of microcirculation is due to the fact that blood circulation is an integral component of healthy biological tissues, providing the cells of the body with everything they need. Abnormalities in the development of vascular system are related to various pathologies, including cancer. A number of presently developed methods of cancer therapy are based on destroying exactly these vascular neoplasms ('antiangiogenic therapy methods'), which distinguishes them from more traditional methods targeted at the cancer cells themselves. In connection with the appearance of these approaches and a number of other biomedical problems, the study of OCT capabilities for three-dimensional (3D) visualization of blood microcirculation in vivo became a problem interesting from the scientific point of view and very important for biomedical applications, the solution to which turned out to be not simple at all.

The problem of blood circulation imaging is also solved based on other known methods of medical visualization. We can mention here computer tomography (CT) with the use of contrasting agents, magnetic resonance (MR) angiography, and Doppler ultrasonic methods. Many optical approaches are also being developed, including Doppler methods for flow measurements, laser speckle contrast visualization, methods of diffuse correlation spectroscopy, and in vivo fluorescence microscopy [32–35]. In recent years, great progress has been observed in the development of optoacoustic-based angiography [36], including studies in Russia [37, 38]. Each of the mentioned approaches has its advantages and drawbacks in terms of invasiveness, complexity, spatial resolution, contrast, sensitivity, probing depth, the necessity of using contrast agents, as well as the possibility of assessing the field of flow velocities and some parameters of the assumed blood circulation model or imaging only the geometry of the vascular network, etc. Blood flow visualization methods use a certain contrast mechanism that allows distinguishing the blood flow from the biotissue surrounding blood vessels. Of particular interest are methods that require no contrasting agents and are based on using the intrinsic motion of scatterers in the bloodstream. Such contrasts are used in approaches to implementing OCT angiography based on the Doppler effect and various methods based on assessing the variability of the speckle patterns (both amplitude and phase) of OCT images.

3.1 Doppler approach

It is known that the component of blood flow velocity parallel to the optical beam axis induces a Doppler frequency shift in the backscattered signal:

$$f_{\mathrm{D}} = k_0 \frac{V_z}{\pi} . \tag{3}$$

Here, k_0, as above, is the central wave number of the field (with the tissue refractive index taken into account), and V_z is the axial component of the blood flow velocity. Usually, the total velocity magnitude V_{t} is of interest, related to V_z via the Doppler angle θ_{D}, $V_z = V_{\mathrm{t}} \cos\theta_{\mathrm{D}}$. However, to find V_{t}, it is required to determine experimentally the Doppler shift f_{D} and the total spatial geometry of the blood flow, which is rather problematic. For typical values of blood flow velocity in microvessels of the order of fractions of 1 mm s^{-1}, the Doppler frequency shift, according to Eqn (3), amounts to a few kilohertz. Measuring such small frequency shifts directly in the frequency domain is problematic for broadband OCT radiation [39]. In this connection, in practical implementations of the Doppler approach, the phase change $\Delta\varphi$ of the OCT signal between the scans described by expression (2) is used. By the known time interval Δt between them, the desired velocity component $\Delta\varphi/\Delta t \propto \Delta z/\Delta t = V_z$ is estimated. To reach a sufficient accuracy, it is necessary to average the phase variations over a certain ensemble of pixels. A more detailed discussion and examples of microvessel imaging by this method can be found in review [40] and original papers [41–43]. It is important that, for a correct estimation, the phase variation between the scans must not exceed the total period 2π.

However, there are methods, Doppler-based in their essence, that yield no quantitative characteristics of flow velocities, but use the Doppler effect to distinguish the signals from the vessels with blood flow from the surrounding static tissue. Here, we can mention the power Doppler approach [39, 44, 45] and optical angiography [42, 46–49] — their general principle is the division of spectral bands, corresponding to the contribution from the moving blood and tissue, assumed to be immobile but in reality exhibiting various physiologically determined motions. Determining the optimal parameters of such separation is a difficult problem because of the overlap of ranges of the separated signals, due to which the effective filter also removes part of the desired blood flow signal. Generally, the 'power' options of Doppler methods, in contrast to the quantitative phase-resolving ones, ensure due to averaging a higher sensitivity in detecting small 'slow' vessels at the cost of losing quantitative information about the velocity magnitude. Sometimes in this case it is possible to save information about the velocity sign and construct an image of the vascular network with color encoding of the blood flow direction [50].

3.2 Correlation approach in optical coherence tomography angiography

The correlation approach in optical coherence tomography angiography does not require contrast agents either and is also based on the selection of the motion of scatterers in the blood flow (vessel section regions) in by-depth two-dimensional scans sequentially obtained at the unchanged position. Note that repeated OCT scans were also required for implementing the Doppler approach, the pairwise comparison usually being insufficient to get a satisfactory signal-to-noise ratio, so that at each position it is necessary to record series of three to six or more scans. A 3D image requires two to three orders of magnitude more 2D scans. Due to these reasons, the processing of such data and the very process of obtaining them require a long time, which is still admissible in experiments with immobilized animals but unacceptable for the examination of humans. Therefore, great attention was attracted by methods in which the analysis requires a possibly smaller number of scans for comparison, approaching pairwise processing. One such option was the angiographic visualization of the correlation type, based on finding the correlation coefficient between pairwise compared pixelated scans with the use of a small enough window 2×2 or 3×3 pixels in size. With a large enough interval between the frames, the images of the scatterers in the vessel flows considerably change, decreasing the interframe correlation, whereas for the regions of 'hard' tissue the similarity of images is higher and, correspondingly, the correlation coefficient is higher. For maximum contrast in terms of the correlation level, the interval between frames should be not too small (so that the scatterers in the flow would have enough time to move) but not too large, so that the image of the background tissue would not have time to change significantly. The approach testing showed its operability [51], but, in recent years, other options for selecting the inherent motions of blood particles have become more widely used. The implementation of these options is intended to simplify the processing itself, weaken the requirements for immobilization of tissues, and increase the efficiency of numerical stabilization of images during their analysis; notably, there is a tendency towards using a pure intensity signal [52].

3.3 Angiography based on temporal variability of speckle intensity in optical coherence tomography

An illustrative example of the OCTA method is an angiographic approach based on the use of variability in the speckle pattern of OCT images (often referred to as the speckle-variance approach, SV-OCTA). The approach also requires comparing a few, $n = 1, \ldots, N$, two-dimensional images of the tissue in depth (B-scans), sequentially obtained at one position, in which for each pixel the intensity variance I is evaluated:

$$\mathrm{SV}_{ij} = \frac{1}{N} \sum_{n=1}^{N} (I_{nij} - I_{ij}^{\mathrm{mean}})^2 . \tag{4}$$

Here, i and j are the coordinates of pixels in the lateral and axial direction, N is the number of scans compared, usually, $N = 2-10$, and I_{ij}^{mean} is the pixel intensity averaged over N scans [53]. Usually, the interframe interval is a few tens milliseconds, during which the blood particles in the vessel section noticeably change position or are even replaced with other particles, so that, in contrast to Doppler methods [53], the vessel direction relative to the beam axis practically plays no role, which is an advantage of the method. However, a complicating circumstance for reaching a good vessel contrast is the necessity to provide sufficient stabilization of the living tissue surrounding the vessels, which is, as a rule, far from static due to physiological reasons (breathing, heartbeats, etc.). For such stabilization in experiments with animals, for example, special containers are used that have windows fixed at the skinfold on the back of a mouse or a rat (Fig. 5a). In the region immobilized by such a window, series of B-scans are recorded, in which, using the SV method, sections of vessels are selected for the chosen B-scan position. By changing the positions of the B-scans, it is possible to form a three-dimensional data array

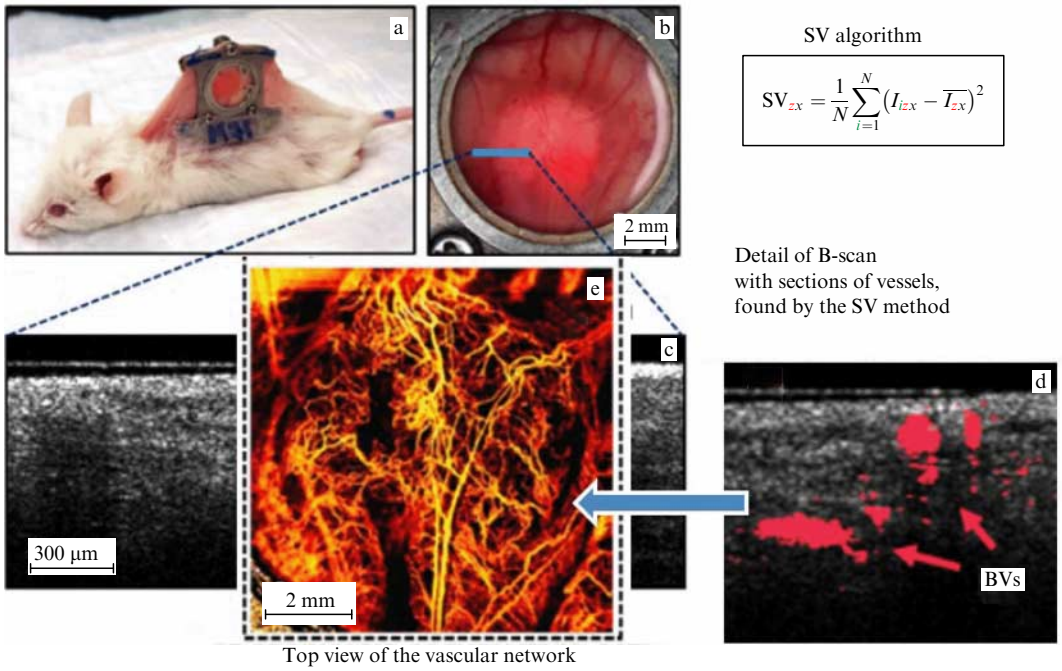

Figure 5. Using the SV method to visualize the vascular network. (a) Laboratory animal with a tissue-immobilizing window. (b) Magnified image of the window with a blue segment, along which the repeated depth B-scans are recorded. (c) Example of the original structural depth B-scan. (d) A part of the B-scan with sections of blood vessels (BVs) selected by the increased level of intensity variance in a set of N B-scans recorded in the unchanged position. (e) Resulting en face projection of the vascular network. (Adapted from [55].)

with the image of the microvascular network. Then, for the convenience of perception, it is possible to project the three-dimensional data from the set of B-scans on a horizontal plane, obtaining a top view (referred to as a C-scan). By combining such scans, it is possible to obtain images of a fairly large area (in Fig. 5, the C-scan size is 8×8 mm). Such a version of OCTA is widely used in research, above all, in experiments with animals under narcosis with reliable immobilization of the studied area using windows, when the angiographic imaging can be implemented by postprocessing and there are no strict requirements for the examination speed. Various modifications of the SV method, including those using a variation in not only intensity but also the phase [54], are some of the most popular means of studying microcirculation.

3.4 Method using high-pass filtering to extract the signal variability in vessels

The method of filtering to extract the signal variability in vessels was proposed for implementing in OCT devices produced by IAP RAS and began to be actively used in PRMU and a number of collaborating clinical centers. When developing the method, the task was to ensure its performance without immobilizing windows, even in animal studies, with the prospect of application in humans. An important task was also to reduce the examination time. To this end, it was necessary to find a way not to literally apply a stepwise shift of stacks of compared B-scans (resulting in significant time loss due to transient processes in the micromechanical elements that control scanning) but to use partial overlap of A-scans during the smooth scanning of the position of the optical beam with sufficient self-overlap. It was also necessary to ensure sufficient compensation of the intrinsic masking movements of the living tissue without immobilizing windows.

One of the variants of this approach was based on recording sufficiently dense B-scans, in which A-scans in the lateral direction would overlap several dozen times [56]. In such scanning, immobile scatterers that fall into the region of self-overlapping of A-scans form a strongly elongated spot-speckle, while, in the vessel flow, because of the motion of scatterers, a chain of laterally short speckles is formed in a similar self-overlap region. A part of a real record in Fig. 6a illustrates this difference in the lateral variability of speckles. Of importance is also the compensation for masking movements, which at a small interval between A-scans manifest themselves mainly in the pixel phase change. In contrast to local motions in vessels, the masking movements are larger-scale, shifting A-scans practically as a whole (in this case, mainly the vertical component of displacements affects the pixel phase). Thus, it is possible to find a change in the phase of the adjacent depth-averaged A-scans and to correct it at each pixel of the next scan (as Fig. 6b schematically shows). At the same time, in sections of blood vessels, the local phase variations, independent of the large-scale motions, will not be compensated for. Such a compensation of the motions of the tissue surrounding the vessels has shown itself to be rather efficient when working with lab animals, removing the necessity of stabilizing windows. The resulting image consisting of speckles with substantially different lengths in the lateral direction can be subjected to Fourier filtering, removing in the spectral domain the low-frequency components that correspond to the elongated speckles of the 'hard' tissue (Fig. 6c). After the inverse Fourier transform, in the newly obtained image, only the vessel sections with small-scale speckles should be retained (Fig. 6e). Finally, having a set of such scans, corresponding to a three-dimensional volume, it is possible to construct an en face projection (top view) with an additional labeling of blood vessels from different depths by different colors (Fig. 6f).

Note that the execution of direct and inverse Fourier transforms with intermediate filtering of the low-frequency

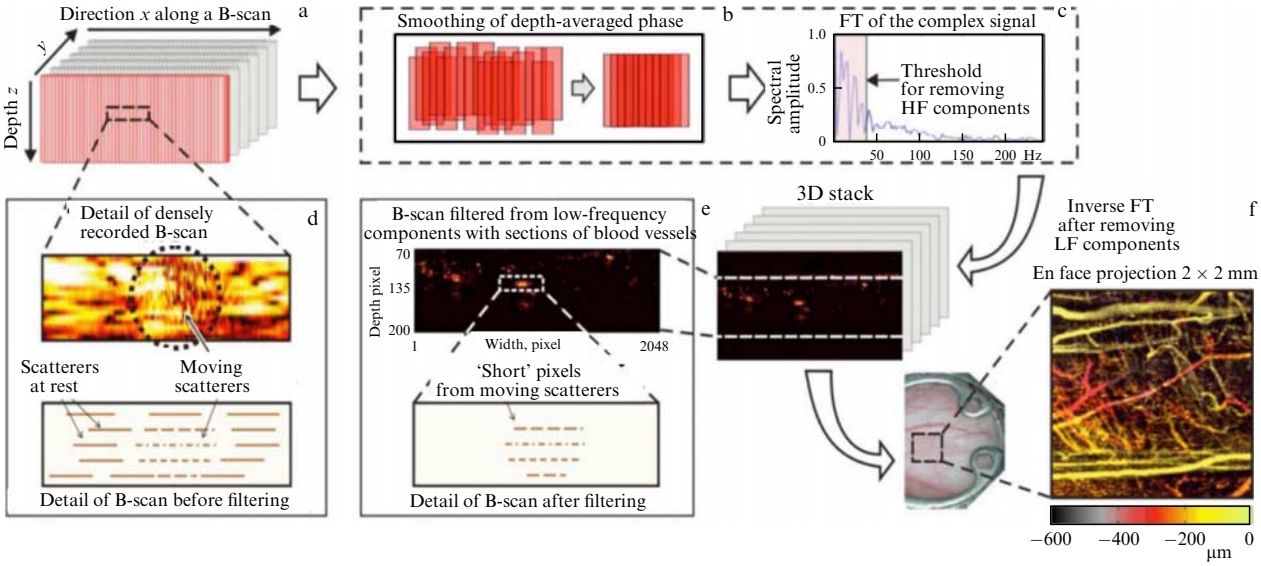

Figure 6. Illustration of the principle of high-frequency filtering of densely recorded OCT images and phase compensation of masking vertical displacements of A-scans. FT — Fourier transform. (Adapted from [56].)

part of the spectrum, according to the properties of the Fourier transform, is equivalent to a convolution of the initial image with a function whose spectrum determines the transmission band shape of the high-pass frequency filter. Such a function should actually cover only the region of overlap of the compared A-scans, which enables constructing the filtered image of vessels in a sufficiently local way, in fact, immediately for every portion of overlapping scans.

The next step in the development of the considered approach was the creation of a version of OCT angiography, capable of imaging in real time and applicable for examining human patients [57]. Of primary importance was the transition from the contactless regime to the one with contact, although the 'contactless' regimes usually required using special windows (as shown in Fig. 5a) or other methods of immobilization to suppress the masking movements of a living biotissue. In the implementation [57], to eliminate large-scale masking movements, it was proposed to use the contact of an OCT probe with the examined tissue. However, because of the pressure of the output probe window, deformations and, therefore, displacements inhomogeneous in depth arise in the tissue, masking the blood flow and requiring a modification of the compensation method. For this purpose, instead of 'pulling' the entire A-scans compared, as with translation displacements, in the case of strain-induced displacements, such a correction should be performed to a different degree, depending on the depth [57]. The better-stabilized position of the tissue with respect to the probe in the contact regime instead of comparing adjacent A-scans within one B-scan allowed for comparison of the corresponding A-scans in sequentially recorded B-scans. The interval between B-scans is a few tens milliseconds (which is hundreds of times greater than the interval between the adjacent A-scans). Therefore, the blood particles have time to move substantially between each pair of B-scans. Their plane in the course of scanning slowly displaces, providing a partial overlap of 5–6 B-scans when getting volumetric data. The execution of sliding convolution, equivalent to high frequency filtering, makes it possible to visualize the vascular network immediately in real time during the acquisition of 3D data.

In recent years, the described approach to angiographic imaging has been actively used in biomedical studies carried out at PRMU and other medical centers in Nizhny Novgorod, mainly to solve problems related to oncology. As compared to postprocessing, the developed method, capable of controlling microcirculation imaging in real time, eliminated a significant percent of poor-quality records and sharply accelerated and simplified the examination by removing the necessity for immobilizing windows. All the above factors are of primary importance, since multiple OCTA examinations are required to obtain statistically significant results in one biomedical investigation.

For example, in studies with model tumors [58–60], based on observing the disappearance of microcirculation in the tumor during the first 24 hours after a photodynamic therapy (PDT) procedure, it was possible to establish a criterion for a long-term forecast of the tumor response to the procedure. It is important to emphasize that, in contrast to a number of other methods not using the motion of blood particles (and using, for example, the selective absorption of light by blood hemoglobin, as in optoacoustic angiography), OCT angiography visualizes the vascular network exactly by the presence of blood flow (Fig. 7). Of course, using OCTA, in addition to qualitative assessment of images, it is also possible to quantify the parameters of the microvascular network and to formulate quantitative criteria (performing skeletonization and assessing the total length per area unit, including a selective study of contributions from the thinnest capillaries of a single-pixel thickness that differ from thicker vessels by their reaction).

Even more important is that the angiographic imaging in real time can be used not only in laboratory experiments but also in patients [61, 62]. For example, in Ref. [61], in patients subjected to radiation therapy of oral cavity cancer, by changes in the blood flow characteristics on the inner surface of cheeks determined by OCTA imaging, it was possible to reveal signs of mucositis (a radiation therapy complication) even before the appearance of its explicit painful symptoms and to begin preventive therapy. Examples of OCTA images obtained in patients [61] are presented in Fig. 8. Using this OCTA method developed at IAP RAS, which competes well

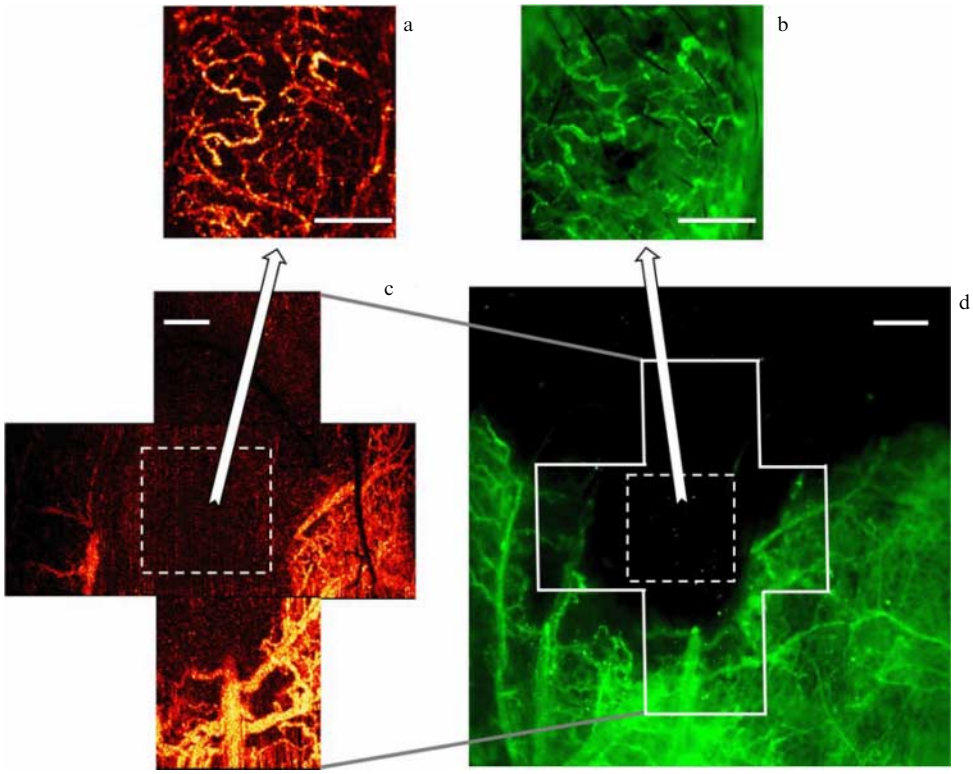

Figure 7. Confirmation of correct visualization of blood flow stoppage in vessels by comparison with visualization using a fluorescent contrast agent (FITC combined with dextran (2 MDa) (Sigma, USA)). (a, b) OCTA image and fluorescence image of blood flow in the tumor center before PDT procedure. (c, d) OCTA image and control fluorescence image of the tumor center and its periphery 24 hours after PDT, demonstrating that the blood flow vanished. Size of the scale bars is 1 mm. (Adapted from [59].)

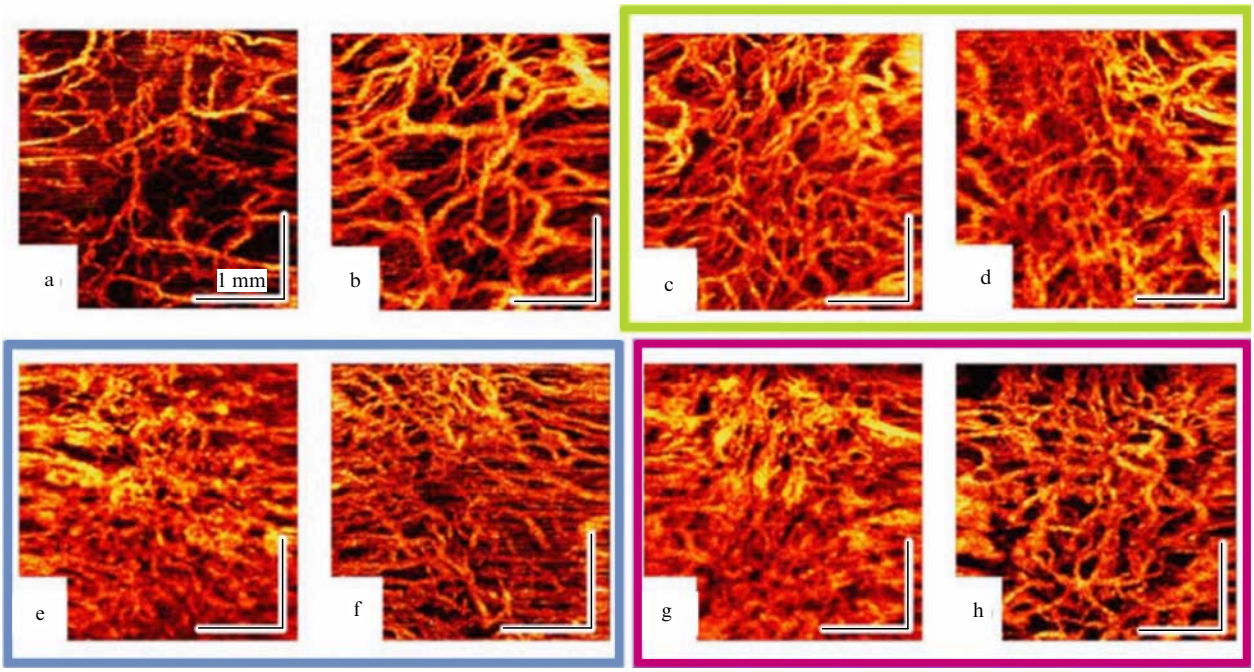

Figure 8. Examples of OCTA images of blood flow on the inner surface of a patient's cheek obtained using the OCTA method based on high-frequency filtering with angiographic visualization in real time. Angiograms demonstrate that the blood microcirculation substantially changes both after radiotherapy, provoking mucositis, and in response to anti-mucositis therapy. (a) Typical angiogram before radiotherapy. (b) Angiogram after irradiation (dose of 8 Gy), in which an increase in the density of vessels is already seen, although mucositis signs still do not visually manifest themselves in patients. (c) Mucositis of the 1st degree (dose of 10–12 Gy). (d) Analogous angiogram after the beginning of anti-mucositis therapy. (e) Mucositis of the 2nd degree (dose of 14 Gy). (f) After the beginning of anti-mucositis therapy. (g) Mucositis of the 3rd degree (dose > 20 Gy). (h) After the beginning of anti-mucositis therapy. (Adapted from [61], where a quantitative analysis of angiograms in terms of the total density of vessels in an angiogram and selective assaying of the total length of capillaries with a diameter of < 15 μm are also carried out.)

in robustness with the methods developed by other groups, has already led to world-class results in biomedical studies carried out at PRMU and collaborating medical centers with the support of physicists.

Concluding the present section, we note that the improvement in procedures and methods of angiographic processing of OCT images continues towards reducing the requirements for physical immobilization of the region studied and increasing the efficiency of compensating for masking movements. In the nearest future, this will open up even a wider range of OCTA applications, including those in combination with the elastographic OCT modality [60], discussed in Section 4.

4. Principles of optical coherence elastography and examples of its use

Optical coherence elastography (OCE) is an emerging modality modality, the development of which is considered one of the most important and promising lines of OCT progress [2]. As mentioned in the Introduction, the history of OCE can be thought to have begun with paper [18] (1998), in which it was proposed to translate to OCT the elastographic approach [17] successfully developed at USI. The main motivation for elastography's development is the very high contrast between soft tissues differing in the shear modulus (varying by a few times and even a few orders of magnitude between different tissues or even different conditions of one type of tissue). These are exactly the differences revealed by palpation, known for ages, which allows detecting various tumors in soft tissues by the subjective perception of their increased stiffness. Although in practically all soft tissues ultrasound waves possess a weakly varying velocity of ~ 1500 m s^{-1} (in fact, insensitive to the shear modulus of the tissue and determined mainly by the compression modulus of the saturating water), US imaging allowed objective assessment of the differences in shear modulus using additional mechanical impacts on the tissue. This radically increased the informativeness and diagnostic value of USI, particularly for applications in oncology. It is interesting that, even before the appearance of elastographic visualization prospects, the very term elastography as a method of characterization of tissue stiffness had been, apparently, introduced by Soviet authors, who in the 1970s used mechanical loading devices to study the elastic properties of biotissues [63].

After the revival of the term elastography in USI and OCT in Ref. [18], in analogy with Ref. [17], it was proposed to visualize mechanically induced quasistatic deformations based on the analysis of series of OCT scans and then draw conclusions related to the elastic properties of biotissues. However, it took almost 15 years of effort to get breakthrough results in the realization of this idea. In Sections 4.2–4.6, the main focus is exactly on the quasistatic approach, above all the original and in many ways still unparalleled option for its implementation, proposed at IAP RAS. However, to complete the OCE development picture, in Section 4.1, we briefly also dwell on alternative approaches used in OCT elastography.

4.1 Optical coherence elastography based on measuring the velocities of shear and surface waves

Note that the idea to use USI to measure the velocities of shear waves and thus implement elastography was proposed in the late 1990s and included the participation of Russian physicists [64]. Then, this field was most actively explored by French researchers [65], and in the 2010s the wave approach became available on a few commercialized platforms and entered the practice of clinical diagnostics. In this approach, to generate shear waves, the transformation of longitudinal US waves under the action of an intense focused ultrasound beam on a tissue is used. The propagation of secondary shear waves (which in soft biotissues have a velocity two or three orders of magnitude smaller than the propagation velocity of longitudinal US waves, ~ 1500 m s^{-1}) is also visualized by US probing. Then, from the measured propagation velocity, the shear modulus is evaluated.

In the 2010s, similar principles were tested to implement OCT elastography (see review [66] and references therein). In this case, the perturbations produced by the shear waves are rather simple to visualize using the interrelation between the phase variations and the axial displacements in the wave field (see Eqn (2)). Practically speaking, because of an imaging depth much smaller than in the USI, the wave OCE more frequently does not use the volume shear waves [67] but surface waves, in particular, Rayleigh waves, whose velocity is only slightly less than that of bulk shear waves [68]. Also, for shear waves propagating obliquely with respect to the optical beam axis, there is an axial strain component, giving rise to phase changes in the optical signal. It is possible to choose the directions, amplitudes, and phases of a pair of crossed beams of shear waves such that, in the region where their fields overlap, only the longitudinal component of the polarization will be observed. Such a construction, also proposed to implement the wave OCE, is called a 'longitudinal shear wave' [69], although, of course, it is not a wave eigenmode of the probed medium.

An important advantage of the wave approach is the sufficient simplicity of its noncontact implementation. This is of particular interest for investigating such 'delicate' tissues as the eye cornea or lens [70, 71], although to date such manipulations have been performed almost exclusively on extracted eyes or eye tissue samples with the use of air pulses or pulses of focused ultrasound to excite the probing waves [66].

One more attractive feature of the wave approaches was the expected simplicity of obtaining quantitative estimates of the shear modulus from the measured shear wave velocity. In the case of surface waves, such expectations were justified in phantoms having a thickness large enough to consider the medium a semispace and the surface wave a nondispersive Rayleigh wave [72]. However, the real thickness of the cornea is only a few hundred micrometers; there is an almost liquid vitreous body immediately under it and a lens at a depth of about 1 mm. Under such conditions, the wave modes are substantially more complicated than nondispersive Rayleigh waves, and, if the model is chosen inadequately, the measurement data interpretation can lead to large errors. Providing spatial resolution along the surface when using surface waves is not related to fundamental difficulties, but for high enough accuracy, an appropriate free path length is needed which restricts the resolution usually to a few hundred microns, which is much poorer than the initial resolution of the structural OCT patterns. Enabling resolution in the depth direction is more problematic here. Studies in this area, as well as those generally aimed at improving the correctness of interpretation of wave measurement data in the wave OCE, are being actively continued (see, e.g., [66, 73]).

We can also note that, in recent years, demonstrations of other options of wave OCE have appeared. For example, in Ref. [74], in the studied samples (biosimilar phantom and extracted eye cornea), using a vibrating contact indentor, a reverberation field of shear waves with known frequency but superposing at random angles was excited. By means of OCT, the structure of the reverberation field was visualized, and the wave number was evaluated from the scale of spatial correlation. From the known wave number, it was possible to evaluate the velocity and shear modulus with the spatial resolution allowing the detection of shear modulus inhomogeneity in a cornea. Note that such an approach resembles the tomographic methods developed in seismic science based on detection and correlation analysis of the inherent noise seismoacoustic fields in the depths of Earth [75], although in Ref. [74] only the directions of the waves, rather than the frequency, were random.

Another option, even closer in a sense to 'noise tomography,' was demonstrated in recent paper [76], where, in a layer of a specially prepared phantom sample inhomogeneous in the horizontal direction, a noise field of surface waves was excited and visualized by OCT. Then, also using a correlation method, the wave number was evaluated in various regions, which allowed visualizing the inhomogeneities of the shear modulus in the horizontal direction. Some other options of exciting auxiliary mechanical perturbations, sometimes rather exotic (like using the Lorentz force when a tissue sample is placed in a magnetic field and a current is excited in it through applied electrodes) are considered in review [77].

In Sections 4.2–4.6, the main focus is on another fundamental area in the development of OCE, the so-called compression approach, the possibility of implementing which in OCT was initially discussed back in 1998 [18]. However, practically workable implementations of this approach and the corresponding demonstrations of important biomedical applications have appeared only in the last 5–6 years.

4.2 Compression optical coherence elastography and strain visualization in optical coherence tomography

First, let us recall that the tensors of elastic stress σ_{ij} and strain ε_{ij} in the traditional approximation of a linear isotropic medium are related as

$$\sigma_{ij} = \frac{E}{1+v}\left(\varepsilon_{ij} + \frac{v}{1-2v}\,\varepsilon_{kk}\delta_{ij}\right). \tag{5}$$

Here, E and v are the elasticity modulus and the Poisson ratio of the medium, respectively, δ_{ij} is the Kronecker symbol, and summation is carried out by subscript k. For sufficiently small deformations, the strain tensor is expressed in terms of the derivatives of displacements by the known formula

$$\varepsilon_{ij} = \frac{1}{2}\left(\frac{\partial u_i}{\partial x_j} + \frac{\partial u_j}{\partial x_i}\right), \tag{6}$$

where u_i are the displacement components.

The Young modulus E in Eqn (5) and the shear modulus G determining the velocity of shear waves (measured in the wave elastography) are related via the Poisson ratio:

$$E = 2\,(1+v)\,G\,. \tag{7}$$

Note that, with the exception of stiff bone tissue, for the overwhelming majority of tissues, from jelly-like substances (with an E modulus of the order of a few kPa) to cartilage (with $E \sim$ a few MPa), the Poisson coefficient with high accuracy is very close to the value $1/2$, characteristic of liquids. Therefore, for practically all biological tissues, Eqn (7) reduces to the expression

$$E = 3G\,. \tag{8}$$

Due to such proportionality, moduli E and G are equivalent from the viewpoint of diagnostic value, so that, instead of assessing directly the shear modulus G in elastography, the Young modulus E can be estimated, which determines the reaction of the medium to the application of a longitudinal uniaxial stress. Indeed, if the stress has only the component σ_{11}, then, taking into account the known relation $\varepsilon_{22} = \varepsilon_{33} = -v\varepsilon_{11}$ corresponding to the definition of the Poisson ratio [78], Eqn (5) for soft biotissues takes the form

$$\sigma_{11} = 3G\varepsilon_{11} = E\varepsilon_{11}\,. \tag{9}$$

Therefore, instead of directly studying the tissue response to shear strains, it is possible to use the longitudinal uniaxial load of the tissue to obtain equivalent elastographic information. Then, Eqn (6) for the strain reduces to

$$\varepsilon_{11} = \frac{\partial u_1}{\partial x_1}\,, \tag{10}$$

so that to estimate ε_{11} it is enough to find only the longitudinal displacement u_1 and its axial derivative. Therefore, below, we will omit the indices denoting the axial displacements and strains as u and ε, and the axis x_1 directed into the depth of the tissue will denote as z.

Exactly such an idea of using a uniaxial load (compression) of a biotissue was proposed for implementing the USI elastography in Ref. [17], where it was also noted that, when pressing on tissue with a flat piston, a nearly uniaxial stress is created around it if the medium motion is not restricted in the lateral directions. As a piston, it was proposed to use the USI probe itself. A schematic diagram of such method, called compression elastography, is presented in Fig. 9.

J Schmitt [18] proposed, by analogy with ultrasound, to transfer this idea to the OCT elastography implementation. As is seen from Eqn (9), for the quantification of modulus E, not only the values of the local axial strain ε (which can be found by analyzing the OCT scans of a deformed tissue) but also the value of the axial stress σ_{11} should be known. One can try to assess this stress by measuring the force applied to the tissue by an OCT probe with the known contact area. However, in Refs [17, 18], it was noticed that, if at some depth the Young's modulus is known, then to find it at another depth, as is clear from Fig. 9, one can use the equality of elastic stresses at different depths:

$$\sigma = E_1\varepsilon_1 = E_2\varepsilon_2\,, \tag{11}$$

from which it follows that

$$\frac{E_1}{E_2} = \frac{\varepsilon_2}{\varepsilon_1}\,, \tag{12}$$

i.e., the visual distribution of strains actually yields the relative distribution of the inverse Young's modulus (below, for brevity the Young's modulus will also be referred to as the stiffness). Therefore, to implement the compression OCE (C-OCE), the key step is to restore the local axial strains in the biotissue.

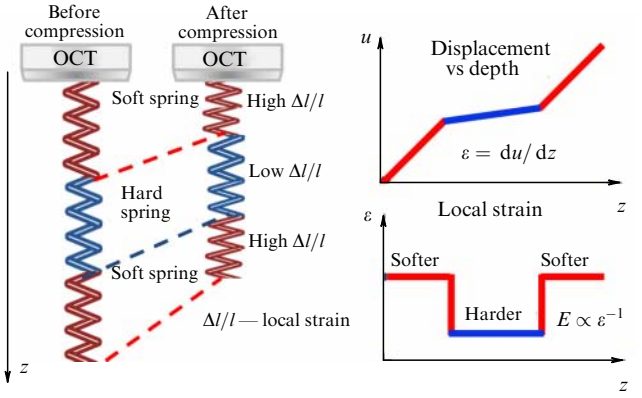

Figure 9. Basic diagram of measuring strains in compression elastography, proposed in Ref. [17] to implement USI elastography.

4.3 Correlation approach in optical coherence tomography

To realize the correlation approach at USI, it was proposed first to find axial displacements based on the cross correlation of the medium scans before and after deformation. In this case, to enable spatial resolution, the operation of correlating pixelated images had to be executed within a certain window, whose size is relatively small compared to the total size of the scan, although such a correlation window must contain sufficiently many (several ten or more) independent image elements to ensure the accuracy of the correlation maximum determination. In application to USI scans and the analysis of photographs of deformed samples in engineering applications [79], the correlation approach turned out to be quite workable, so that, starting from Ref. [18], attempts to implement it in OCT were made, for example, in Refs [80–82]. However, in general, these studies showed an insufficient efficiency of the correlation approach due to the unsatisfactory accuracy of reconstructing the field of displacements and, all the more, the subsequent numerical differentiation to evaluate the local strains. Particularly, in contrast to photographs with an artificial pattern, in OCT scans the speckles arise as a result of the interference of fields from subresolution scatterers located in a sample volume of the optical beam with the axial length determined by the coherence length, which usually exceeds the wavelength by an order of magnitude if the OCT system is not super-broadband as, for example, in Ref. [83]. Therefore, the OCT speckles usually demonstrate very high sensitivity to various movements of subresolved scatterers (which is exploited in OCT angiography as discussed in Section 3). However, such variability, manifesting itself as the 'boiling' and blinking of speckles under medium deformation, strongly deteriorates the accuracy of the correlation determination of local displacements. A detailed quantitative analysis of the corresponding limitations is carried out in Ref. [84].

As an advantage of the correlation method, we can note the possibility in principle of finding both lateral and axial components of displacements, although, as mentioned above, it is exactly the axial displacements that are of major interest in implementing compression elastography. In this connection, although some authors continue to consider the possibilities of correlation determination of displacements in OCT (see, e.g., [85–88]), the main trend in the development of C-OCE became the use of the phase approach that enables efficient searching for the axial displacements. This approach presently dominates in compression OCT elastography, which has demonstrated very interesting results in recent years.

4.4 Phase approach to visualization of displacements and strains in optical coherence tomography

As noted in Section 4.2 when discussing Eqns (5)–(12), a very attractive feature of the compression approach is the use of only the longitudinal component of the strain to solve the problem of evaluating the Young's modulus (and, hence, the shear modulus). In this regard, it is natural to try to use interscan phase variations that are the most sensitive to the longitudinal displacement of scatterers (similar to the predominance of the longitudinal Doppler effect over the transverse one).

An important step toward the OCT evaluation of local strains was made in Ref. [89]. Since, according to Eqn (10), the axial strain is determined by the gradient of displacements, $\varepsilon = \partial u/\partial z \propto \partial(\Delta\varphi)/\partial z$, the problem of evaluating the strain reduces to finding the axial gradient of interframe phase variations. In Ref. [89], the local gradients of the phase variations (and, hence, strains) were evaluated using the mean square regression of the observed dependence of interframe phase variations on depth in a certain interval. To reduce the contribution of low-amplitude and, therefore, particularly noisy pixels in OCT scans, in [89] it was additionally proposed to introduce amplitude weighting.

Note also that the phenomena of 'blinking' and 'boiling' of speckles in the deformed medium lead to random variations in their amplitudes (i.e., both an increase and a decrease in the signal level may occur, depending on the random initial positions of scatterers in each pixel). These amplitude random variations reduce the interframe correlation and substantially deteriorate the quality of correlation tracing of displacements. However, the change in the speckle phase upon deformation have a more regular character, since, even at a random variation in the scattered signal from a group of subresolved scatterers, the signal phase varies in a more regular way in accordance with the displacement of the entire group (although, due to the 'leakage' of scatterer images into the adjacent pixels, some randomness, of course, is also present). Nevertheless, the phase variations described by Eqn (2) turn out to be substantially more robust with respect to deformation-caused decorrelation effects, which is confirmed by both analytical arguments and numerical simulation [40, 90].

However, another problem arises in the phase method of strain evaluation. Obviously, in Eqn (2), for displacements greater than $\lambda_0/2$, the phase variation is measured with an ambiguity of an integer number of periods 2π. For OCT scans with typical depths of $\sim 10^3$ μm and $\lambda_0 \sim 1$ μm, already at moderate strains within a range of $10^{-3}-10^{-2}$ the displacements are superwavelength and there is a strong ambiguity in phase variations in a considerable part of the scan. One of the approaches to the assessment of such superwavelength displacements commonly accepted in OCT is the summation of small incremental interframe displacements not exceeding $\pm\lambda_0/4$ [91, 92], which is often difficult due to the necessity to increase the rate of acquired scans. Another variant, when in deformed tissue adjacent to the OCT probe the displacements arise from zero values, is to remove the phase ambiguity by adding an integer period, if the measured variation of phase exhibits jumps between $\pm\pi$ [93], as shown in Fig. 10. The quality of such phase unwrapping can be strongly deteriorated

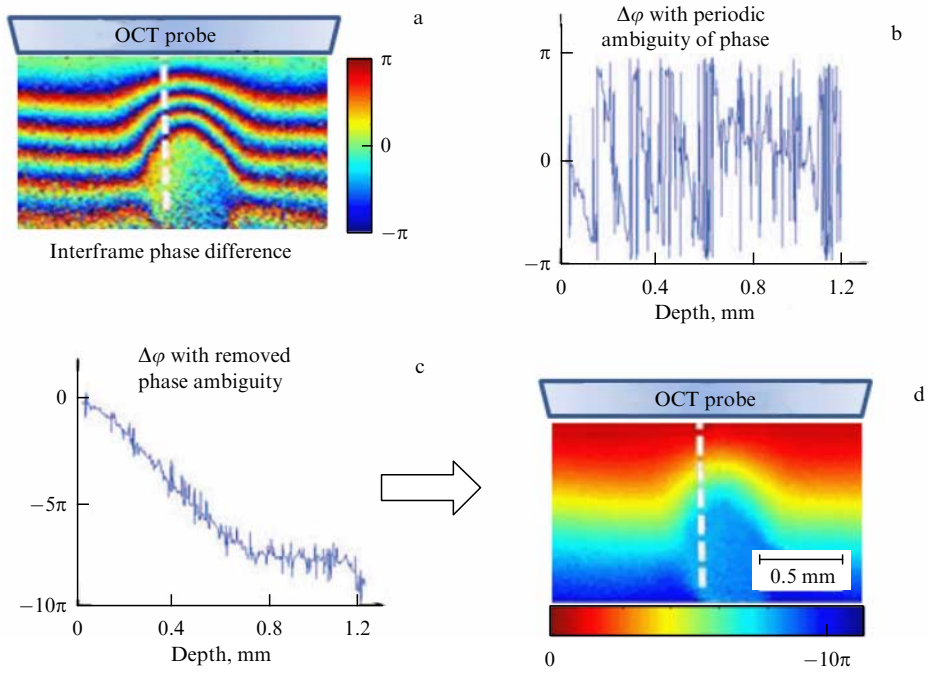

Figure 10. Examples of color-encoded phase variations under tissue deformation (a, d) and the depth dependence of interframe phase change for original phase changes in the original form without (b) and with (c) phase change ambiguity.

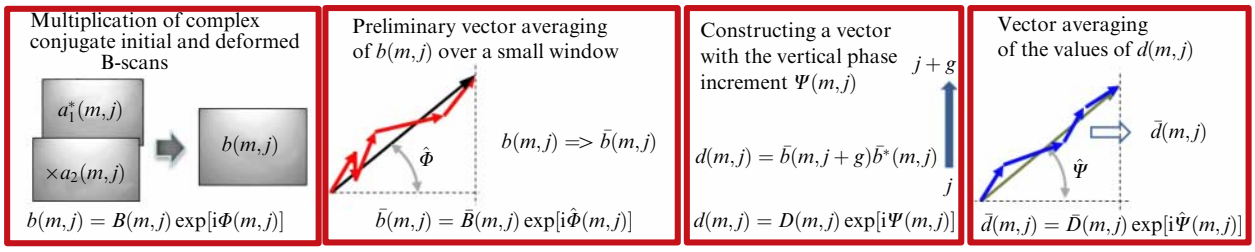

Figure 11. Diagram of a sequence of stages of the evaluation of the axial phase gradient in the vector approach. All intermediate transformations are performed with complex signals, considered vectors in the complex plane, and the desired axial phase gradient $\hat{\Psi}$ is extracted only at the very last stage. (Adapted from [96].)

by noise and introduce noticeable errors upon numerical differentiation.

However, for the main goal of compressive OCE — to find the local strains — the phase unwrapping can be unnecessary. Namely, the derivative $\varepsilon = \partial u/\partial z \propto \partial\varphi/\partial z$ can be evaluated by the observed phase variations even if the phase variation is ambiguous to an integer number of periods (as in Fig. 10a, where each rainbow stripe corresponds to one period of phase variation). In this case, it is important to ensure that, within the depth interval in which the gradient of phase variation is evaluated, the displacements of particles differ by less than $\lambda_0/2$ (respectively, the phase changes by $< 2\pi$). Such a method of searching for the local gradient of phase variations is discussed in more detail in Refs [89] and [94], where it is also shown that superwavelength displacements can be reconstructed by depth summation of the displacements, corresponding to the local strains found without the necessity of phase unwrapping in the visualized range of depths. The development of such approaches actively continues [92].

The next essential step in the development of the phase method of OCT strain evaluation was the 'vector method' [95, 96]. The name is such because in this method all intermediate operations with the OCT signals are executed in vector form in the complex plane, and the signals themselves with amplitude A and phase φ are presented in the complex form as $A\exp(i\varphi) = A\cos\varphi + iA\sin\varphi$. The stages of operating with complex pixel amplitudes in vector form are illustrated in Fig. 11. In the vector method, as in the least-square method [89], the phase variation gradient is evaluated depending on the depth within a chosen small rage of depths. Additional averaging (also in complex form) over the horizontal coordinate in a small region of a few tens of micrometers is also very efficient to improve the signal-to-noise ratio (SNR).

The vector method retains the advantages of amplitude weighting and allows 'automatic' suppression of the greatest phase errors of $\sim\pi$ radians in the measured phase increments. Indeed, as is seen from Fig. 11, the vectors with the greatest phase errors ($\sim\pi$ rad) do not affect the direction of the resulting vector, evaluated by averaging over the processing window. The vector method does not require removing the phase ambiguity and demonstrates enhanced robustness with respect to noises (both the

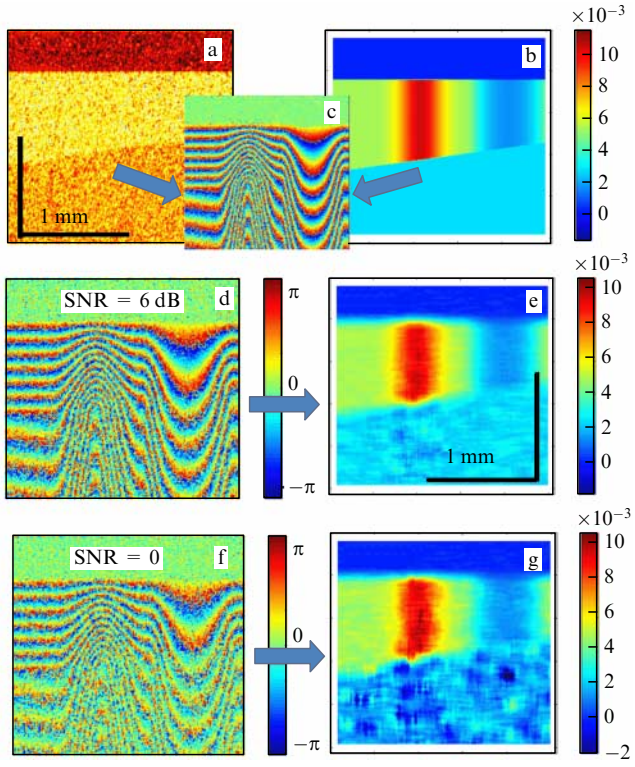

Figure 12. Modeling OCT scans in the case of inhomogeneous strains based on the model [24, 29] and their reconstruction by the vector method [96]. (a) Structural image with differently deformed layers, selected by different colors. (b) Strain distribution specified in the model. (c) Interframe phase variations, corresponding to the strain field shown in Fig. b, in the absence of measurement noises but considering the 'decorrelation noise,' especially noticeable in the region of maximum displacements at large depths. (d–g) Analogous variations in phase upon imitating strong measurement noises with the signal-to-noise ratio being 6 dB or even 0 dB and the results of reconstructing the strain field, agreeing well with those initially specified, shown in Fig. b. (Adapted from [96].)

additive measurement noise and the 'decorrelation noise'). One more advantage of the vector method is high computational efficiency, which is important for real-time strain imaging [97]. It is no coincidence that, after paper [96], the vector method began to be actively used by various teams developing OCT elastography [93, 98–100]. Note that convenient and computationally efficient models of the OCT scan formation [24–29], mentioned in Section 3, became a very important instrument in the development of the vector method and in other studies, which required a detailed clarification of amplitude-phase changes in the OCT signals caused by the movements of scatterers.

Figure 12 illustrates the robustness of the vector method by the example of numerical modeling performed in Ref. [96]. At large depths, i.e., in the region of maximum displacements, the model scans are seen to manifest blurring of the rainbow isophase lines due to 'decorrelation noise.' Moreover, Gaussian noise was additively incorporated (imitating the noises of receiving elements) with a mean intensity corresponding in Fig. 12d to a rather low (6 dB) SNR and even a zero SNR (i.e., when the mean intensities of the image and noise are equal) in Fig. 12f. Nevertheless, even with such noisiness, the strains reconstructed using the vector method (Fig. 12e, g) are in satisfactory agreement with the strain field initially specified in simulations (Fig. 12b) [96].

4.5 Experimental examples of strain imaging in optical coherence tomography by the vector method

Starting from Ref. [18], in the literature the term *elastography* is rather often understood, besides mapping the elastic properties, as visualizing displacements and especially the local strain field. Such visualization is not only an auxiliary operation in the study of elastic properties of biotissues but is also of more general interest, allowing the study of the strain dynamics of very different origins: thermomechanical processes, osmotically induced strains, strains caused by intrinsic stresses, drying processes, etc. For example, rapidly varying thermomechanical-origin strains in such collagen tissues as the eye cornea or cartilage tissue can be studied under heating with an IR laser. Interest in these phenomena is due by the fact that, upon making the appropriate choice of pulsed irradiation mode, moderate heating can be nondestructive. On the other hand, it may already be sufficient to induce temporal breaking and reconnection of intermolecular bonds and thus enable changing the shape of the exposed tissue, which is important in the context of developing novel nonsurgery technologies for correcting the shape (and refractive index) of the eye cornea [101, 102] and reshaping of cartilage tissues (including *in vivo* techniques, e.g., for correcting the nasal septum shape) or imparting the required shape to cartilage implants used in otolaryngology and maxillofacial surgery [103, 104].

Until recently, there simply were no technologies capable of visualizing such thermomechanical strains in tissues on scales from a few ten micrometers to a few millimeters or investigating the impact of the spatiotemporal mode of irradiation. In recent studies carried out jointly by the Institute of Applied Physics of RAS and the Institute for Photon Technologies of RAS, the capabilities of the developed C-OCE method for studying such processes were demonstrated [105–108]. Figures 13a–c show examples of thermomechanical strains developing in the extracted cornea of a rabbit eye during the first second from the beginning of irradiation by a beam of an IR laser, reconstructed by the vector method. The irradiated sample had a sandwich structure, in which the cornea was placed between buffer layers of soft biosimilar silicone with a known Young's modulus (a structural OCT image of such a three-layer assembly is shown in Fig. 13d). The buffer silicone layers, as explained below, were used to study the variations in the biotissue Young's modulus caused by irradiation.

Figure 13e shows in the 'waterfall' form how at a depth of about 100 μm from the surface the distribution of interframe strains evolves in time, depending on the horizontal coordinate. The complex spatial strain distribution in Fig. 13e, in addition to Figs 13a–c, demonstrates that the strain development is determined not simply by the local temperature but also by the combined impact of spatially different fields of temperature and thermomechanical stresses, whose maxima lie on the slopes of the temperature distribution. As the process goes on, this leads to the appearance of maximum interframe strain on the slopes of the temperature distribution, rather than directly in the region of maximum temperature. Similar effects were revealed in studies of thermomechanical impacts not only in the eye cornea but also in cartilage tissue, also consisting mainly of collagen [107, 108]. Figures 13f–g for a cartilage sample exposed to a heating beam with a Gaussian profile show, like Fig. 13e, that the maximum interframe ('instantaneous') strains, as well as the summed interframe, i.e., accumulated (cumulative) strains,

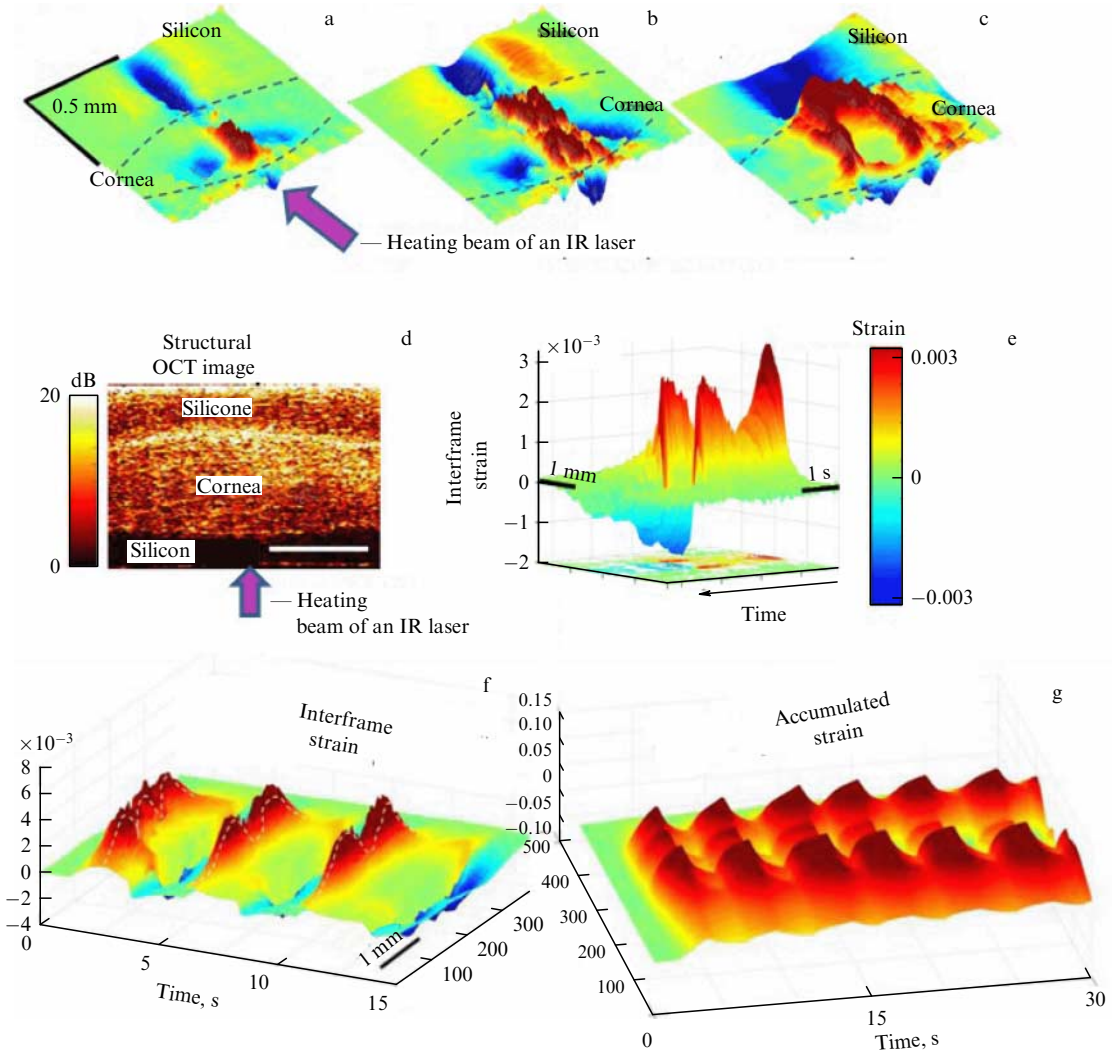

Figure 13. (a–c) Examples of 'instantaneous' interframe maps of spatially inhomogeneous strain fields arising at different stages of laser heating an extracted rabbit eye cornea placed between two silicone layers and subjected to irradiation by an IR laser (such strains are studied in the context of new nonsurgical technologies of changing the cornea's shape). (d) Structural image of silicone–cornea–silicone. (e) Time evolution of interframe cornea strain in the central part of heating area. Images for (f) interframe and (g) accumulated (by summation of interframe values), or cumulative, strain show very similar features of the laser-induced strain evolution in a cartilage sample. By the example of three heating pulses, Fig. f shows that only at the very beginning of heating are the largest strains localized in regions of maximum temperature on the beam axis; then, strain maxima shift to the slopes of the temperature distribution, where thermomechanical stresses are maximum. (A more detailed discussion and other examples can be found in Refs [106–108].)

gradually move from the heating beam axis to the periphery, where the thermomechanical stresses rather than the temperature are maximum, which facilitates the breaking of intermolecular bonds. Understanding such features opens up possibilities of reaching the required changes in the sample shape at a lower temperature by optimizing the heating beam geometry, which minimizes biological damage to the tissue [108, 109].

For example, consider ring-shaped autoimplants intended for implanting in the trachea, fabricated from a plate of costal cartilage from the patient themselves in the course of operation [110]. In this case, the laser heating of a mechanically bent sample leads to partial destruction and reformation of molecular bonds between collagen fibrils, causing the relaxation of internal mechanical stresses which stabilized the shape imparted to the sample. If the relaxation is insufficient, the implant can slowly unbend (in fractions of an hour) with consequences dangerous for the patient. The exposure required for sufficient relaxation is substantially variable and depends on the cartilage condition (the patient's age, plate thickness, etc.). Therefore, it is of primary importance to have an objective and fast (giving the result in about 1 min) method of intraoperative control of a sufficiently stable implant. The described method of quantitative OCT strain imaging opens up such a possibility: in a few ten seconds, it allows detecting slow, still visually unnoticeable deformation of the sample beyond the acceptable limits, which points to the necessity of additional irradiation of the fabricated implant [111]. Moreover, the joint use of visualization of the accumulated information and the changes in the Young's modulus in the exposed region also allowed a characterization of microstructural changes that occur in tissue on scales directly unresolved in OCT images [107, 112, 113].

Thus, the developed method of OCT deformation imaging is of interest for studying both sufficiently fast (on a scale of fractions of a second) and slow (on a scale of several hundred or thousands of seconds) deformation processes. In

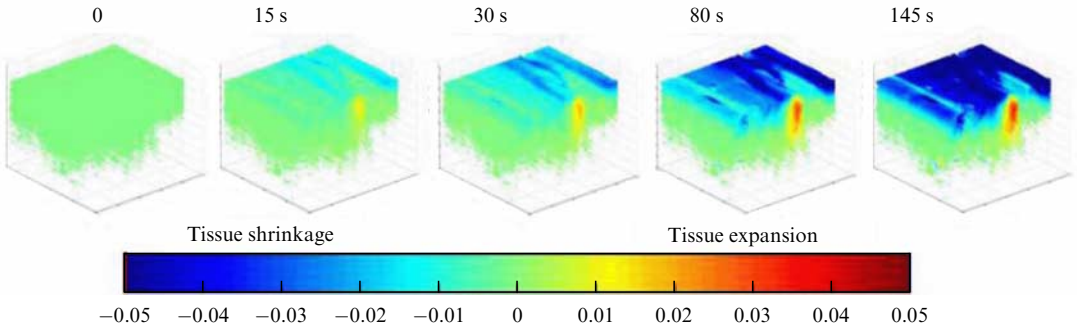

Figure 14. Example of three-dimensional visualization of strains developing in near-surface layers of a cartilage sample upon its drying (negative strains are shown in blue); simultaneously, in the region subjected to preliminary local pressure, there is a relaxation expansion (red color).

the latter case, it may be necessary to optimize the regimes for obtaining and processing it both to increase the signal-to noise ratio and to avoid recording multigigabyte data, absolutely excessive for such tasks [114]. For such sufficiently slow processes, it is admissible to reduce the time resolution to a few seconds or more, making it possible to perform the analysis of the entire three-dimensional blocks of data without using high-speed OCT facilities and to get a detailed spatiotemporal picture of the process development. An example of this kind of three-dimensional visualization is presented in Fig. 14.

One more area in which the development of strain imaging opened up unavailable earlier possibilities is the investigation of deformation processes of osmotic origin, which occur, for example, when using various nonisotonic solutions, as in Ref. [115] where, using OCT, deformation processes were studied in cornea samples intended for implantation and initially impregnated with a conservation agent that was then removed in the course of which tissue deformations due to osmotic effects must be controlled. In recent years, among the substances demonstrating osmotic activity, significant attention attract the so-called optical clearing agents [116]. The impact of such agents on biotissues (both *in vitro* and *in vivo*) is used to reduce the optical scattering in biotissues and to increase the optical field penetration depth, which is important for various methods of optical diagnostics and phototherapy [117]. The agents used for the above purposes can substantially differ in osmotic properties, including the concentration dependence (e.g., for glycerol solutions). In this connection, recent papers [118, 119] demonstrated for the first time the possibilities of OCT strain imaging for the characterization of nontrivial spatiotemporal dynamics of osmotically induced strains. It is expected that soon the developed methods of OCT strain imaging will find new applications related to the rapidly developing methods of tissue engineering.

4.6 Quantification of stress–strain curves and Young's modulus of biotissues

Methods of strain mapping based on phase-sensitive OCT in combination with the compression principle allowed efficient implementation of the idea of visualizing elastic properties of biotissues, ensuring their quantification based on proportions of the form (11) and (12) applied to incremental strains. Knowledge of the tissue initial load degree at which the incremental strains are determined is extremely important for correct interpretation of the estimated values of the Young's modulus. This is because many biotissues, especially neoplasm tissues, demonstrate pronounced elastic nonlinearity, so that their modulus may vary by several times at strains of a few percent, which is small for biotissues.

For practical implementation of the quantitative C-OCE, it was proposed to place on the surface of the studied biotissue a thin layer (a few hundred microns thick) of a transparent [120] or weakly scattering [121] soft (biosimilar) silicone-type plastic with a known Young's modulus (Fig. 15a). For a transparent precalibrated reference layer, its depth-averaged strain can be assessed by the change in the total thickness using the boundary-tracing algorithm [120]. In the case of a weakly scattering layer, its strain is evaluated like that of the biotissue [121] (usually by means of the computationally efficient vector method; see Fig. 11). An important advantage of the considered option is the spatial resolution of the strain, which can be strongly inhomogeneous in the bulk of the precalibrated layer, although the mechanical properties of the layer are homogeneous. In particular, the inhomogeneity can be due to the distorting influence of stiction of the precalibrated layer to the surface of the loading probe. Indeed, to ensure that it is exactly the Young's modulus that determines the elastic response of the compressed precalibrated layer, its material should be able to move freely in lateral directions; then, the elastic stress near the probe will be close to the expected uniaxial one. The stiction/friction at the contact between the pressing stiff surface and the silicone can give rise to a substantial contribution from lateral components of the elastic stress. In other words, there arises a tendency toward bulk compression, the response to which is characterized by the bulk modulus K, which exceeds the Young's modulus by a few orders of magnitude, $K \gg E$, i.e., the effect of stiction looks like a significant increase in the layer stiffness and, respectively, a decrease in its deformability.

Figure 15b presents an experimental example demonstrating that in a homogeneous layer the stiction effect leads to an increased separation between isophase lines (which corresponds to a decreased value of strain near the contact with the probe). The reconstructed strain profile in Fig. 15c illustrates the same effect: near the contact with the loading probe at insufficient sliding, the strain in homogeneous silicone appears to be highly (nearly fourfold) underestimated. After adding a drop of saline for lubrication at the silicone-glass contact, the strain in the layer appears to be already close to homogeneous (Fig. 15d). For quantification of the elastic stress in the layer and, correspondingly, correct determination of the biotissue modulus, such control of stiction effects is very important.

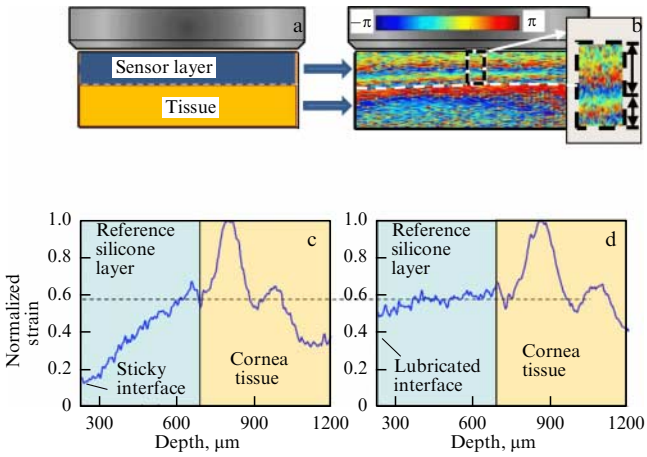

Figure 15. Using a weakly scattering layer as a stress sensor. (a) Schematic diagram of the experiment, in which a sample of a rabbit eye cornea is placed under a silicone layer. (b) A real example of the interframe phase change, demonstrating the inhomogeneity of the phase change due to silicone sticking to the silicone-glass interface. (c) Example of the depth profile of the normalized (to the maximum) strain showing a decrease in the strain level inside the homogeneous silicone due to the effect of silicone sticking to the output window of the probe. (d) A similar more homogeneous profile of strain in silicone, when the sticking is reduced by adding a drop of lubricating liquid at the interface. (Adapted from [121].)

In addition, the soft precalibrated layer placed between the tissue and the compressing stiff surface plays yet another important role: smoothing possible inhomogeneities of the stress and strains at the tissue-glass interface in the case of an imperfectly planar tissue surface. Even when the height of irregularities seems insignificant (a few ten microns), their manifestations can be unexpectedly strong. At the initial stages of loading, the tissue deforms first in convex regions, whereas, in concave regions, the axial strain can not only decrease but even change sign due to the tendency of soft tissues (with a Poisson ratio close to 0.5) to preserve their volume under deformation. This can lead to rough errors in the evaluation of the elasticity modulus of the tissue (see realistic examples in [122]). Using soft precalibrated layers eliminates such artifact manifestations.

Furthermore, for use as optical sensors of elastic stress, an important property of precalibrated silicone layers is their high linearity, which was checked experimentally in a series of studies [121, 123, 124]. The linearity of the layers was confirmed in direct measurements with a force cell, which showed that the ratio of stress and strain increments (i.e., the Young's modulus $E = \Delta\sigma/\Delta\varepsilon$) remains constant in a wide range of strains (several ten percent). It is also possible to demonstrate the very fact of high linearity in a kind of self-calibration test in the compressed sandwich structure of two silicone layers with strongly different moduli, observing a gradual increase in the accumulated strains obtained by summation of small interframe strains for the sequence of OCT scans recorded in the course of material compression. Figure 16a demonstrates that, between such accumulated strains in two stiffness-contrast silicone samples, the linear proportionality is preserved up to strains of about several ten percent. Therefore, the accumulated strain in silicone can with good accuracy be considered proportional to the elastic stress.

For comparison, Fig. 16b shows a similar dependence between the silicone strain (recalculated into stress) and the strain in the biotissue used as the second material (removed breast tumor) [121]. As is seen, for the tumor already at a strain of $\sim 2\%$, the stress-strain dependence is strongly nonlinear, so that its current Young's modulus changes by more than three times. The nonlinear dependences obtained by means of the developed C-OCE method agree well with the known results found earlier in the course of mechanical measurements of biotissue properties using loading setups [125].

Due to such pronounced nonlinearity, to interpret correctly the obtained elastic characteristics of a tissue, it is of primary importance to control the level of stress (pressure) on the tissue at which its elasticity modulus is evaluated and to take into account that at quite moderate strains and pressures the current Young's modulus $E = d\sigma/d\varepsilon$ can change several-fold. Even a comparative statement that the Young's modulus is higher in one tissue than in another can change for an opposite. Further studies using precalibrated layers have also shown that, even within the limits of a single OCT scan only a few millimeters wide, the pressure exerted on the studied tissue can change several-fold because of a number of practically uncontrollable factors (surface irregularities of the samples and precalibrated silicones, surface curvature of real samples, and intrinsic mechanical inhomogeneity). Hence, the visualized inhomogeneous strain field can be related to the elastic properties of a nonlinear biotissue in a very nontrivial way. Therefore, for correct interpretation, it is necessary to clarify the conditions under which the evaluation of the elasticity modulus is executed in different parts of the visualized region, to say nothing of the complexity of comparing the results of different experiments. Information

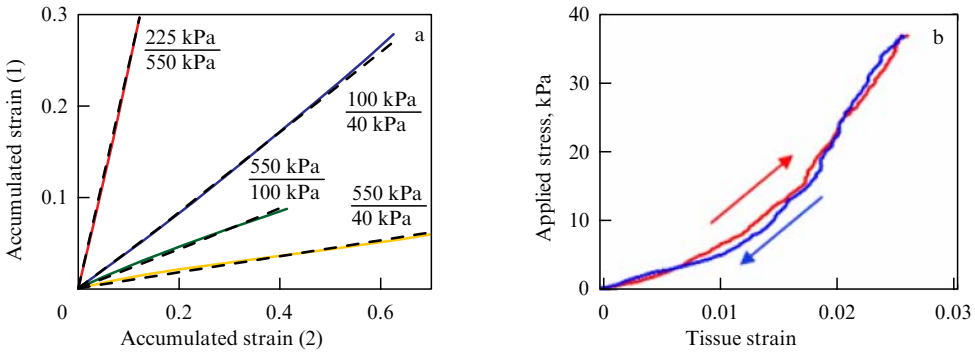

Figure 16. (a) Demonstration of high linearity of silicones, proved by the preserved (under a compression of up to 50–60%) linear proportionality of strains in two layers of a sandwich structure, consisting of silicone with considerably differing stiffnesses. (b) Nonlinear stress–strain curves for loading and unloading a sample of breast cancer tissue obtained by plotting the applied stress (measured through strains of linear elastic precalibrated silicone) depending on strains in the studied biotissue. (Adapted from [121].)

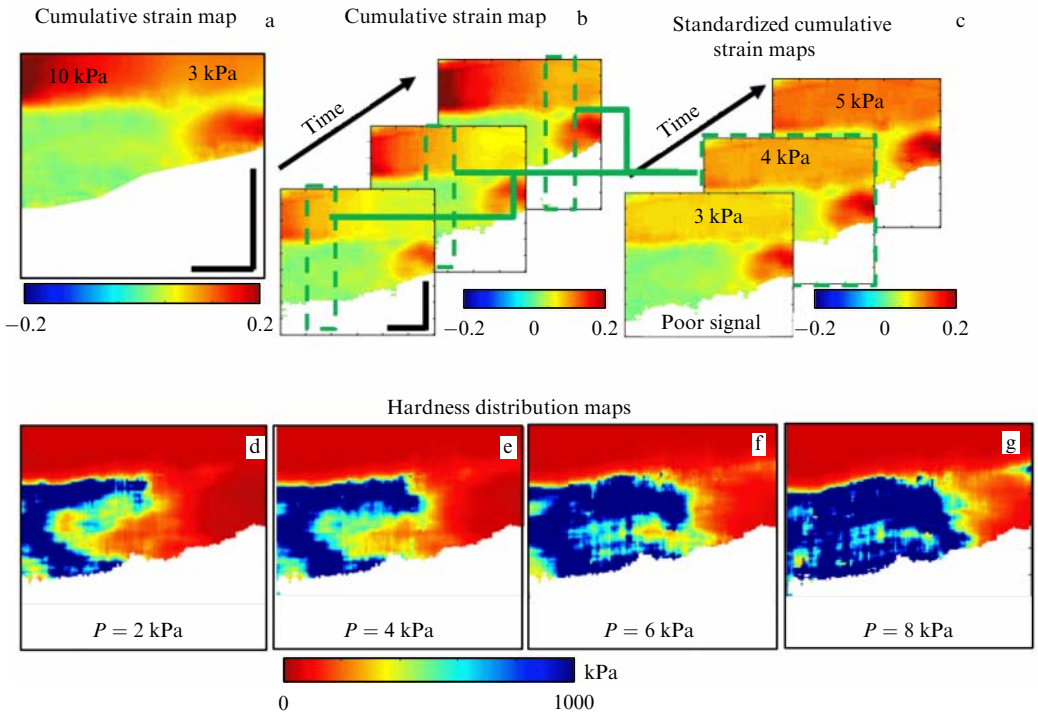

Figure 17. (a) Example of formation of a spatially inhomogeneous cumulative strain distribution and, respectively, nonuniform distribution of pressure in a precalibrated silicone layer, through which the studied breast cancer tissue sample is loaded. Sample is characterized by both an irregular surface and inhomogeneity of the elastic properties in its volume. (b) Schematic image of a sequence of recorded original two-dimensional B-scans of accumulated strain from which vertical A-scans are selected corresponding to the chosen constant level of pressure. (c) Examples of synthesized 'standardized' scans of accumulated strain, for which over the entire area preselected similar values of pressure were provided. Based on such synthesized scans and using Eqn (11), current values of Young's modulus can be evaluated for a particular value of pressure. (d–g) Examples of distribution maps of Young's modulus obtained in this way for different values of pressure on the tissue (indicated in the figure). As is seen, the resultant distributions of the modulus turn to be substantially different upon changing the pressure by a few kPa. Size of vertical and horizontal scale bars is 0.5 mm. (Figure adapted from [124].)

on the mean pressure applied to a tissue sample that can be obtained using force cells (commonly discussed in the literature in connection with such measurements) is absolutely insufficient.

Thus, in the developed C-OCE method, the key is to use precalibrated silicone layers as optical sensors of the local pressure on the tissue in different parts of the scan. Another important feature of the developed C-OCE method is the possibility of obtaining spatially resolved nonlinear stress–strain dependences $\sigma(\varepsilon)$ (like the dependence shown in Fig. 16b for a sample of breast cancer).

To obtain such nonlinear dependences, it is necessary to record a series of OCT scans in the process of tissue compression and for each lateral coordinate to determine the current pressure on the tissue by the precalibrated layer strain and the corresponding spatially resolved values of cumulative strain of the tissue itself. From the found dependences $\sigma(\varepsilon)$, it is then possible to estimate the value of the Young's modulus for the chosen (and thus 'standardized') value of pressure. The Young's modulus can be determined either using a suitable analytical approximation of $\sigma(\varepsilon)$ followed by calculating its derivative $E = \mathrm{d}\sigma/\mathrm{d}\varepsilon$, or by approximating the tangent slope by the chord slope of the experimental curve $E \approx \Delta\sigma/\Delta\varepsilon$ around the chosen 'standardized' value of pressure. The described procedures are illustrated in Fig. 17a–c, and in Fig. 17 d–g examples are presented of how, depending on the chosen value of standardized pressure, the visualized distribution of the elasticity modulus changes in a sample of breast tumor excised during a surgical operation and containing a transition from the malignant tumor to benign surrounding tissue with smaller modulus values. The presented examples show how strongly the visible position of the tumor margin can change depending on pressure and indicate a necessity to elaborate exact quantitative criteria for the correct interpretation of OCE data.

4.7 Quantitative elastospectroscopy based on compression optical coherence elastography for optical biopsy and determination of tumor margins for resection

Due to the limited dimensions of the OCT imaging regions, similar to the examples of using OCT angiography already discussed in Section 3 [58, 59], small-size model tumors, usually inoculated into the ears of laboratory mice, are ideal subjects for the C-OCE method. Such model studies are actively carried out around the world, including at the PRMU Research Institute of Experimental Oncology and Biomedical Technologies, where new possibilities opened up by C-OCE began to be actively studied (including a combination with the OCT angiography discussed in Section 3). One such application of new OCT modalities is related to comparing the efficiency of different methods of therapy, e.g., by chemical preparations with different mechanisms of affecting cancer tumors. Starting from the first test on model tumors [126], C-OCE demonstrated promising qualitative results, namely, in tumor tissues with a high uniformly distributed Young's modulus (several hundred kPa), as the therapy acts and the tumor cells die, zones of decreased stiffness develop till the necrosis of the entire tumor. Such a qualitative visualization, performed *in vivo*, has already turned out to be very useful.

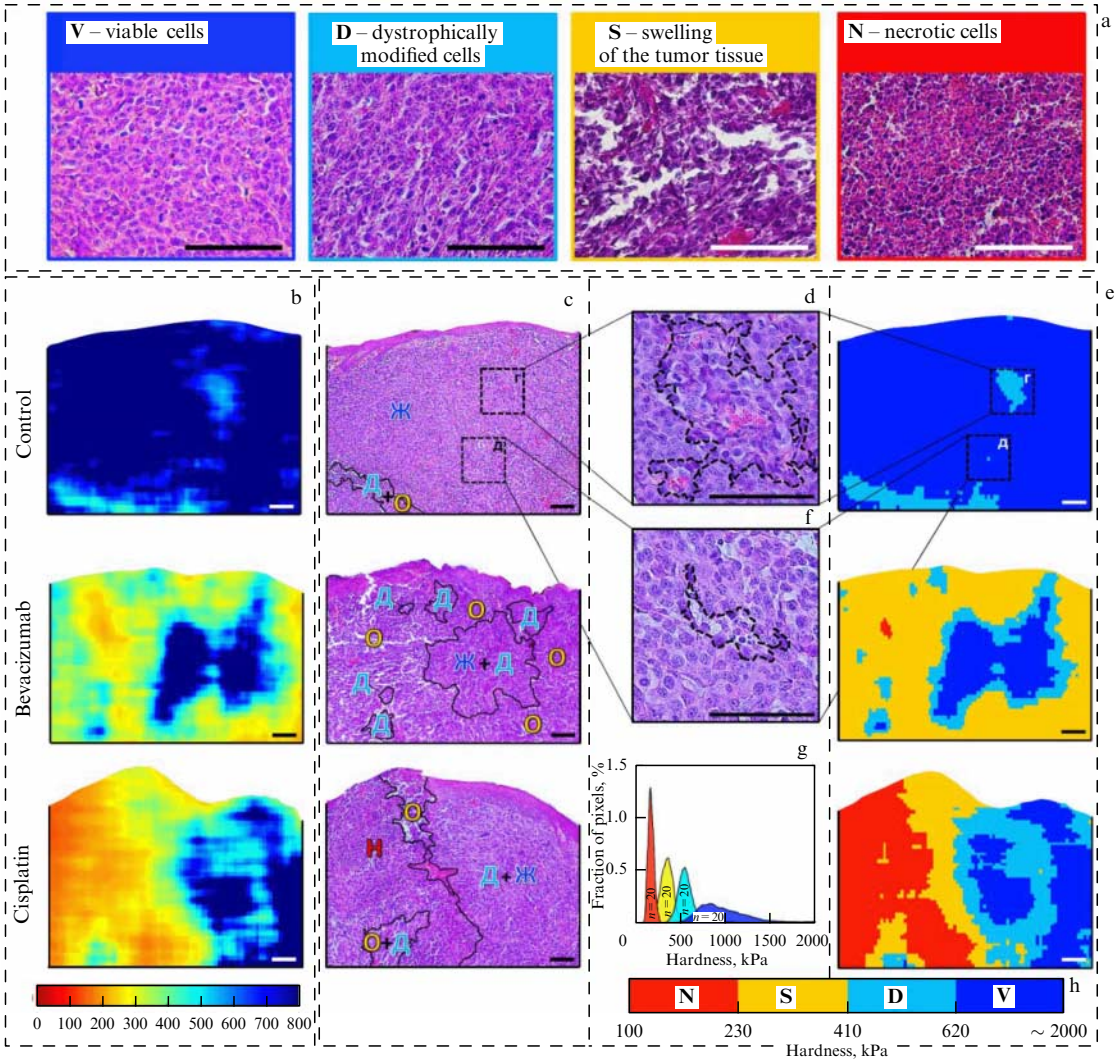

Figure 18. Determination of stiffness absolute value ranges of tumor morphological structures. (a) Magnified histological images of four main morphological components of a tumor. Comparison of stiffness maps (b), obtained *in vivo* on the 7th day after the beginning of therapy (for the control group and groups subjected to treatment with cisplatin and bevacizumab preparations) and corresponding histological images (c); black curves reflect boundaries of morphological structure regions of the tumor. (d, e) Magnified histological areas of the tumor, demonstrating a high sensitivity of the OCE method in detecting small agglomerations of cells, revealing which in a histological examination is difficult. (f) 'Stiffness spectrum' for the four tumor components, in which the bell-like functions correspond to averaged histograms of stiffness values, found using 20 samples for each morphological structure. (g) Color scale and boundaries of stiffness ranges used for automated segmentation of stiffness maps. (h) Segmented OCE images obtained from stiffness maps shown in Fig. b. Size of scale bars in all images is 0.1 mm. (Adapted from [127].)

Developing these results, the authors of Ref. [127] carried out a targeted comparison of preliminarily obtained *in vivo* OCE images and histologic sections of tumors in the same position. As a result of this comparison, characteristic ranges of stiffness were determined for four main components distinguished in the histological images: the viable cancer cells, the dystrophic cancer cells, the edema zone, and the necrosis zone (see series of images in Fig. 18a). It was found that these ranges are rather well separated, forming weakly overlapping peaks, which can be naturally called the stiffness spectrum due to their resemblance to the emission spectra of molecules (see Fig. 18f, where the peak areas in the histogram are normalized to unity). After determining the characteristic ranges of the Young's modulus and choosing the crossing points of the found distributions for threshold values, the initial Young's modulus maps in the C-OCE images of tumors are easily and automatedly segmented into zones, in which the tissue stiffness corresponds to one of the four subtypes of tumor tissue.

Thus, for OCE images of tumors obtained *in vivo*, it became possible to perform automatically morphological segmentation, earlier available only based on histologic specimens (obtained either invasively for biopsy samples in the case of large organisms or after sacrifycing small animals in experiments). In this case, the laborious preparation of traditional histologic specimens themselves requires several days, and their interpretation and segmentation are executed manually by an experienced histopathologist.

For the examples of comparison shown in Fig. 18, it should be specially noted that the coincidence of not only the topology but also the actual shape of the segmented zones when compared with histological images is impossible, since, during OCE examination, the tissue experiences compression, significantly changing its shape (to varying degrees in zones of different stiffness). Moreover, during the multistage preparation of a histological specimen (formalin fixation, dehydration, paraffining, staining), its shape changes even more significantly. For this reason, to quantitatively compare the

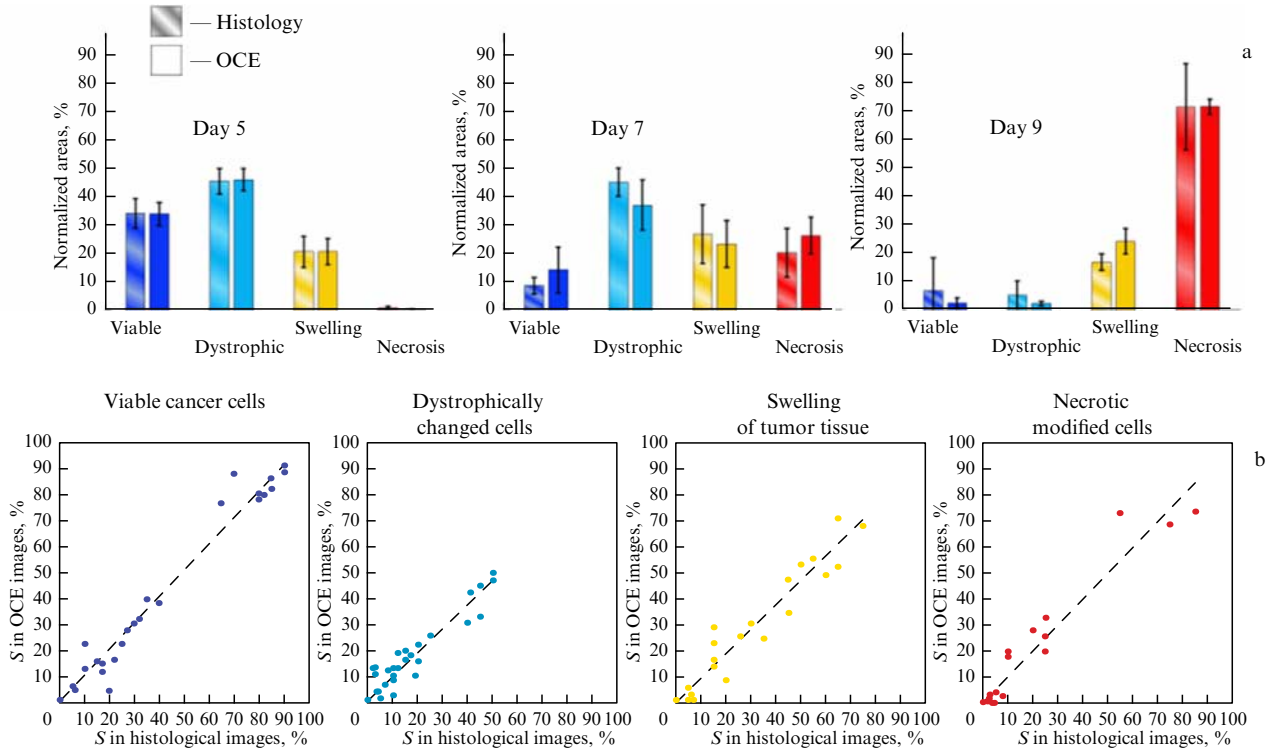

Figure 19. Column diagrams for the areas (S) of histological structures, normalized to the total areas of images, determined by a highly skilled histopathologist from histological images, and automatically segmented in OCE images by the found 'stiffness spectrum.' (b) Correlation dependences between relative areas found using these two methods, which have shown that the correlation coefficient for the areas of all four morphological components lies in the range of 0.94–0.98. (Adapted from [127].)

results of morphological segmentation by two methods, a comparison of relative areas of each of the four components in OCE scans and histological images was chosen. Results presenting the evolution of such areas for a group of mice subjected to chemotherapy (by cisplatin), as well as plots demonstrating the correlation of areas of the morphological components based on histology and elastographic scans, are shown in Fig. 19 (see details in [127]). The observed coincidence of areas of the segmental components turns out to be surprisingly high, with a correlation coefficient of about 0.95 or more.

Thus, although OCT does not provide a resolution of cellular structure (by which the histologist judges tissue subtype), the results of automated OCE segmentation of tissue subtypes demonstrate surprisingly good agreement with conventional histology, considered the 'gold standard.' The ability of OCE not only to perform a binary distinction between tumor and normal tissue but also to carry out quantitative differentiation of four morphological components at once with an accuracy comparable to that in conventional histology, but carried out *in vivo* and almost in real time. This is a unique feature of the developed OCE method inaccessible to previously known methods.

Another unique feature of this segmentation is the possibility of combining *in vivo* OCE studies with OCT angiography, which allows simultaneous *in vivo* monitoring of both morphological and functional changes occurring in tumors during their development and in response to therapy. This possibility was demonstrated in [128], where, in contrast to a comparison of different types of chemotherapy [127], the response of tumors to chemotherapy and photodynamic therapy was compared, characterized by strongly different time scales of tumor response (days or minutes and hours, respectively). The types of model tumors in these studies were completely different (the model of breast cancer in [127] and colorectal cancer in [128]), but, for both types of tumors, both the C-OCE method itself and even the characteristic ranges of stiffness for segmented morphological tissue subtypes confirmed their versatility.

Of course, speaking of the transfer of the obtained results to the examination of patients, we should note that, for example, breast cancer tissues are much more heterogeneous, with significantly different morphological components and other characteristic ranges of the Young's modulus. In addition, a significant limitation, of course, is the relatively small depth of the OCT imaging, especially in comparison with that of ultrasound elastography. Nevertheless, as noted, the sizes of OCT images are quite comparable to typical sizes of histological specimens. In this regard, even without speaking about *in vivo* application in patients, the issue of primary importance is the extent to which OCT examination can replace conventional histology in terms of information content and accuracy, with a very important advantage in the speed and ability to study freshly extracted patient tissue samples. It would be very important to obtain such results comparable to the data of post-operation biopsy directly in the course of operation, which is impossible using conventional histology methods. In this regard, in recent years, methods of accelerated histology using frozen samples have begun to be applied. However, even such an accelerated method is not always applicable in terms of speed for intraoperative use; in addition, its contrast is significantly worse than in conventional histology. Therefore, it is of great interest to develop alternative methods, primarily based on biophotonics, which could, with an accuracy comparable to that of histological methods, control

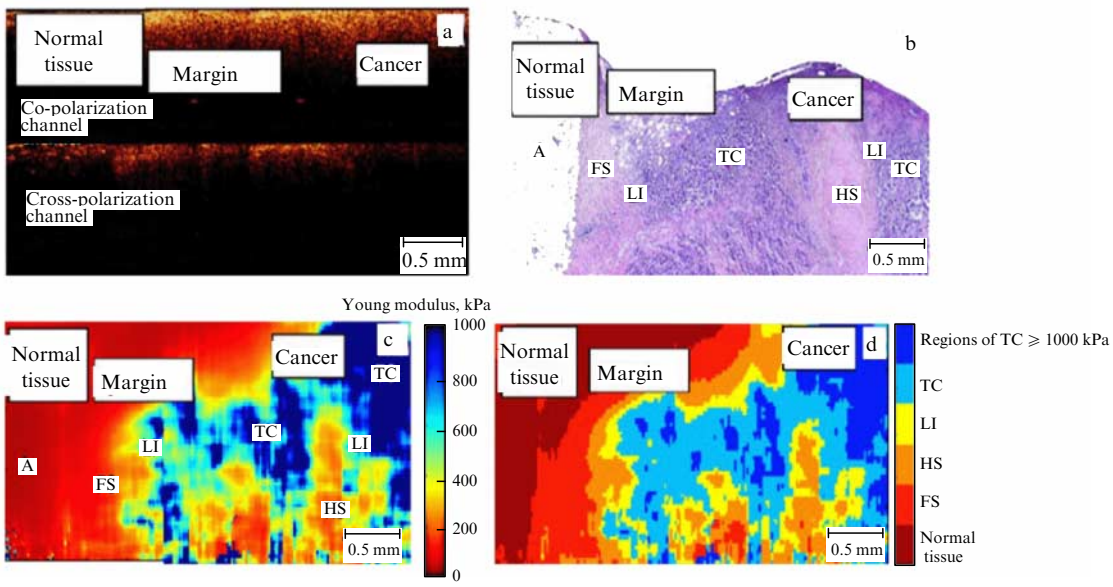

Figure 20. Detailed visualization of the tumor margin by means of the automated segmentation of the OCE image by the difference in the Young's modulus for a cancer tissue sample removed in the course of an operation. (a) Original structural images in two polarization channels (co- and cross-polarization), where the tissue components have no substantial differences in optical properties. (b) Histological image in which five morphological zones of cells are selected: A-adipose and normal connective tissues; FS — fibrous stroma, LI — lymphocytic infiltrate, TC — tumor cells, HS — hyalinized stroma. (c) Young's modulus distribution in the OCE image. (d) Automatically segmented OCE image based on the determined 'stiffness spectrum.' Since the sample shape somewhat changes because of procedures for preparing a histologic specimen and mechanical load during OCE examination, the comparison of histologic and OCE images by literal superimposition of visible detail less than 100 μm in size is impossible in principle. However, the images in Figs b and d perfectly coincide in terms of topology, and high-contrast tumor margin visualization is executed for a few minutes without any special preparation of the tissue, in contrast to visualization by laborious and time-consuming histology. (Adapted from [133].)

the tumor margin for resection as well as determine the degree of its malignancy, at least distinguishing between malignant and still benign forms of tumors.

In this area, in addition to using C-OCE for laboratory experiments, encouraging results have been obtained in recent years both in Russia and abroad, primarily at the University of Western Australia (UWA) in Perth, where the possibilities of C-OCE for detecting tumor margins are also actively studied with the aim of intraoperative use of this new technology [122, 129–132]. Although the studies at UWA are also based on the compression principle with differentiation of tumor from nontumor tissue by stiffness, the distinctive feature of the above OCE approach is the quantitative C-OCE method with standardization of the pressure over the studied area. This is of particular importance for automated morphological segmentation when working with strongly nonlinear breast cancer tissues.

As compared to the above artificially inoculated tumors with a rather simple morphological structure, the tissues of real breast cancer tumors are substantially more heterogeneous in terms of both the morpho-molecular structure and the stiffness properties of the appropriate components. Depending on the classification used, the general name of 'breast cancer' can imply five to six subtypes of malignant neoplasms, strongly differing by the degree of aggressiveness, methods of treatment (often requiring a combination of therapeutic procedures and surgical intervention), and the prognosis of treatment results. In surgery all over the world, more and more attention is being paid to organ-saving operations, in which only the malignant tumor with a minimum margin is removed. However, to exclude relapses after such an operation, the possibility of reliable and executable intraoperatively control of clean tumor resection boundary is very important.

As in the study of model tumors, to solve the problem of clean tumor resection margin control, as well as to elucidate the possibilities of using stiffness differences for identifying subtypes of breast tumors in patients, the elastic properties determined by the developed C-OCE method with the standardization of pressure on the tissue were thoroughly compared with the results of histological examinations of the same areas [133]. In the course of these studies, the characteristic ranges of the Young's modulus were determined for the main morphological components of breast tissues both in the tumor region and in the nearly normal tissues surrounding the tumor. As a result, in the vicinity ± 1 kPa of the standard pressure of 4 kPA, characteristic stiffness ranges were established for the following main tissue components: 1) norm (adiposis + stroma); 2) fibrosis; 3) regions of lymphocytic infiltrate; 4) regions of hyalinosis (developing in cancer tumors); 5) agglomerates of cancer cells, of which the highest values and the broadest distribution of the Young's modulus are usually characteristic. As in the case of model tumors (for which the spectrum of elastic properties is shown in Fig. 18), the distributions of characteristic values of the Young's modulus appeared to be weakly overlapping. This allowed the automated segmentation of C-OCE images, even for breast cancer samples in patients, providing a very distinct differentiation of regions containing cancer cells and the surrounding nontumor tissue.

Figure 20 presents the first example of such automated segmentation of a C-OCE image from Ref. [133]. In addition, in Ref. [133], based on a targeted comparison with histology, the distribution of stiffness properties for nontumor tissues, fibroadenoma-type benign neoplasms, and strongly heterogeneous malignant tumors of various types (in particular, noninvasive ductal carcinoma *in situ* and invasive malignant tumors, lobular cancer — in total, five molecular subtypes of

cancer with different degrees of aggressiveness) were also investigated. In Ref. [133], about 60 samples of various types were examined, and to date such studies have already been carried out for several hundred patients and samples (a number of other examples of OCE examination of breast cancer tumors can be found in Refs [134–137]). These studies have shown that, although different types of tumors do not significantly differ in average clasticity modulus within C-OCE image they show clear differences in the stiffness spectra (in fact, histograms of the Young's modulus distribution over pixelated C-OCE images). Moreover, the significantly higher resolution of C-OCE compared to conventional US elastography also allows using the characteristic differences in the stiffness spatial distribution for differentiation of tumor types (this possibility has also been noted by other authors [131]).

As a result of the analysis, criteria were formulated (including both the measured values of the modulus and the features of its spatial distribution) which make it possible not only to distinguish normal tissue from a tumor but also to differentiate several molecular subtypes of tumors [138]. It is shown that the results based on C-OCE are significantly superior to those of traditional approaches to the analysis of OCT images, even when texture analysis of the conventional structural and polarization-sensitive images are used together. Such traditional approaches continue to be actively used in various groups in the framework of solving more traditional problems of differentiating tumor and nontumor tissues [11]. Regarding the possibility of detecting differences even in molecular subtypes of tumors based on an assessment of their mechanical properties using C-OCE, which has no direct sensitivity to the molecular composition of tissues, as an analogy, we can note the possibility of a quantitative study of the lipid composition of blood serum by mechanical (more precisely, acoustic) spectroscopy [139, 140]. Of course, such acoustic spectroscopy also requires preliminary calibration using standard methods (much more labor-intensive and time-consuming) of biochemical analysis.

In addition to the above-described application related to the imaging of breast cancer tissue [133–138], similar capabilities in both tumor delineation and aggressiveness assessment have been demonstrated for malignant neoplasms (adenocarcinomas) of the intestine [141].

Further studies of the diagnostic use of the capabilities of C-OCE for obtaining nonlinear stress–strain curves of biological tissues are actively continuing [136]. This is of great interest not only in connection with the possibility of reproducible determination of the current Young's modulus of nonlinear tissues at a given pressure level but also in terms of using the nonlinear parameters themselves to increase the sensitivity and specificity of the diagnostic methods based on C-OCE. In a broad sense, there is a physical analogy with using nonlinear acoustic parameters in seismoacoustic diagnostics [142–144]. In some cases, it turns out to be possible to draw directly an analogy between the description of the nonlinear elastic properties of cracky rocks and some biological tissues characterized by the presence of narrow pores/layering in the matrix material, consisting mainly of strands and layers of collagen. Using this analogy with traditional models of fissured media (see, e.g., [145]), it seems possible to draw conclusions about the properties of narrow pores inside the tissue from the experimentally observed nonlinear dependences for collagen tissue of the elastic nonlinear cornea or cartilage tissue. The pores are not yet resolved on OCT scans, but their presence is confirmed by histological images [107, 112]. However, even without relying on model considerations, purely empirically, by targeted comparison of histological images of tumor tissues and their corresponding nonlinear stress-strain curves obtained by C-OCE technology, with the combined use of linear and nonlinear elastic parameters, it turns out to be possible to differentiate tumor tissues with high selectivity, and to detect not only relatively large agglomerates of cancer cells [146] but also areas of their small accumulations, up to scattered single cancer cells [147].

5. Conclusion

The ability of C-OCE to execute express assessment of the aggressiveness degree of tumors and to visualize their boundaries with an accuracy comparable to that of the results of the 'gold standard' of histology on intervals of the order of a few minutes still has no equivalent. From the point of view of developing the physical grounds and the remarkably positive results of testing to solve clinical problems, the new C-OCT modality has already reached the level of development at which it becomes possible to transit to its wide intraoperative use in the clinic. No doubt, the new possibilities of the OCE modality for quantitative high-resolution visualization of both strains and elastic properties are of great interest for biosimilar materials created by methods of tissue engineering or obtained by modifying the initial biotissues. In a number of problems, OCE can be combined with other OCT modalities, such as the OCT angiography discussed above, and polarization-sensitive OCT [12, 60, 138], whose development is considered one of the most important directions of OCT development in the next decade [2, 15].

This study was supported by the Ministry of Science and Higher Education of the Russian Federation within the World-Class Research Centers program (Center of Photonics, agreement no. 075-15-2022-316). The author thanks A A Sovetsky for help in preparing the illustrations.

References

1. Huang D et al. *Science* **254** 1178 (1991)
2. Leitgeb R at al. *J. Biomed. Opt.* **26** 100601 (2021)
3. Gelikonov V M et al. *Radiophys. Quantum Electron.* **60** 897 (2018); *Izv. Vyssh. Uchebn. Zaved. Radiofiz.* **60** 1002 (2017)
4. Schmitt J M, Xiang S H, Yung K M *J. Biomed. Opt.* **4** 95 (1999)
5. Weatherbee A et al. *Opt. Lett.* **41** 2727 (2016)
6. Ge G R, Rolland J P, Parker K J *Biomed. Opt. Express* **12** 4179 (2021)
7. Demidov V et al. *Biomed. Opt. Express* **12** 2952 (2021)
8. Niemczyk M, Iskander D R *Biomed. Opt. Express* **12** 6407 (2021)
9. Moiseev A et al. *J. Biophoton.* **11** e201700072 (2018)
10. Liu Y et al. *Biomed. Opt. Express* **12** 2647 (2021)
11. Zhu D et al. *Biomed. Opt. Express* **12** 3021 (2021)
12. Tuchin V V, Popp J, Zakharov V (Eds) *Multimodal Optical Diagnostics of Cancer* (Cham: Springer, 2020)
13. Gladkova N D, Gelikonov G V, Kiseleva E B (Eds) *Mul'timodal'naya Opticheskaya Kogerentnaya Tomografiya v Klinicheskoi Meditsine* (Multimodal Optical Coherence Tomography in Clinical Medicine) (Moscow: Fizmatlit, 2022)
14. Parker K J, Doyley M M, Rubens D J *Phys. Med. Biol.* **56** R1 (2011)
15. Ormachea J, Parker K J *Phys. Med. Biol.* **65** 24TR06 (2020)
16. Routh H F *IEEE Eng. Med. Biol. Mag.* **15** (6) 31 (1996)
17. Ophir J et al. *Ultrasonic Imaging* **13** (2) 111 (1991)
18. Schmitt J M *Opt. Express* **3** (6) 199 (1998)
19. de Carlo T E et al. *Int. J. Retina Vitr.* **1** 5 (2015)
20. Ikedo T et al. *Biochem. Biophys. Res. Commun.* **495** 332 (2018)
21. Woolman M et al. *Sci. Rep.* **7** 468 (2017)
22. Bachmann A H, Lietgeb R A, Lasser T *Opt. Express* **14** 1487 (2006)

23. Bachmann A H et al. *Opt. Express* **15** 9254 (2007)
24. Zaitsev V Yu et al. *Laser Phys. Lett.* **11** 105601 (2014)
25. Almasian M, van Leeuwen T G, Faber D J *Sci. Rep.* **7** 14873 (2017)
26. Matveyev A L et al. *Laser Phys. Lett.* **16** 085601 (2019)
27. Matveyev A L et al. *Laser Phys. Lett.* **17** 115604 (2020)
28. Matveyev A L et al. *Biomed. Opt. Express* **12** 7599 (2021)
29. Zykov A A et al. *J. Biomed. Photon. Eng.* **7** (1) 010304 (2021)
30. Zaitsev V Yu et al. *Radiophys. Quantum Electron.* **57** 52 (2014); *Izv. Vyssh. Uchebn. Zaved. Radiofiz.* **57** (1) 59 (2014)
31. Turchin I V *Phys. Usp.* **59** 487 (2016); *Usp. Fiz. Nauk* **186** 550 (2016)
32. Yu G et al. *Clinical Cancer Res.* **11** 3543 (2005)
33. Zhang H F et al. *Opt. Express* **14** 9317 (2006)
34. Leahy M J *Microcirculation Imaging* (New York: Wiley-Blackwell, 2012)
35. Dunn A K et al. *Biomed. Opt. Express* **7** 1861 (2011)
36. Karlas A et al. *Photoacoustics* **14** 19 (2019)
37. Subochev P et al. *Biomed. Opt. Express* **11** 1477 (2020)
38. Kurnikov A A et al. *Quantum Electron.* **51** 383 (2021); *Kvantovaya Elektron.* **51** 383 (2021)
39. Yang V X D et al. *Opt. Express* **11** 794 (2003)
40. Zaitsev V Yu et al. *Radiophys. Quantum Electron.* **57** (2014); *Izv. Vyssh. Uchebn. Zaved. Radiofiz.* **57** 231 (2014)
41. Leitgeb R A et al. *Opt. Express* **11** 3116 (2003)
42. Wang R K, An L *Opt. Express* **17** 8926 (2009)
43. Srinivasan V J I et al. *Opt. Express* **18** 2477 (2010)
44. Ren H et al. *SPIE Proc.* **4956** 225 (2003)
45. Kurokawa K et al. *Opt. Express* **20** 22796 (2012)
46. Wang R K et al. *Opt. Express* **15** 4083 (2007)
47. An L, Wang R K *Opt. Express* **16** 11438 (2008)
48. van Soest G et al. *J. Biomed. Opt.* **15** 011105 (2010)
49. Yousefi S, Qin J, Wang R K *Biomed. Opt. Express* **4** 1214 (2013)
50. Wang R K *Opt. Lett.* **33** 1878 (2008)
51. Jonathan E, Enfield J, Leahy M J *J. Biophoton.* **4** 583 (2011)
52. Barton J K, Stromski S *Opt. Express* **13** 5234 (2005)
53. Mariampillai A et al. *Opt. Lett.* **33** 1530 (2008)
54. Mahmud M S et al. *J. Biomed. Opt.* **18** 050901 (2013)
55. Demidov V et al. *Biomed. Opt. Express* **10** 4207 (2019)
56. Matveev L A et al. *Opt. Lett.* **40** 1472 (2015)
57. Moiseev A et al. *J. Biophoton.* **11** e201700292 (2018)
58. Sirotkina M A et al. *Sci. Rep.* **7** 41506 (2017)
59. Sirotkina M A et al. *Sci. Rep.* **9** 6492 (2019)
60. Sirotkina M A et al. *Biomed. Opt. Express* **11** 1365 (2020)
61. Maslennikova A V et al. *Sci. Rep.* **7** 16505 (2017)
62. Gubarkova E V et al. *Sci. Rep.* **9** 18670 (2019)
63. Sapuntsov L E, Mitrofanova S I, Savchenko T V *Bull. Exp. Biol. Med.* **88** 1501 (1979); *Byull. Eksp. Biol. Med.* **88** 740 (1979)
64. Sarvazyan A P et al. *Ultrasound Med. Biol.* **24** 1419 (1998)
65. Bercoff J, Tanter M, Fink M *IEEE Trans. Ultrason. Ferroelectr. Frequency Control* **51** 396 (2004)
66. Zvietcovich F, Larin K V *Prog. Biomed. Eng.* **4** 012007 (2022)
67. Zhu J et al. *Sci. Rep.* **6** 35499 (2016)
68. Viktorov I A *Rayleigh and Lamb Waves*: *Physical Theory and Applications* (New York: Plenum Press, 1967); Translated from Russian: *Fizicheskie Osnovy Primeneniya Ul'trazvukovykh Voln Releya i Lemba v Tekhnike* (Moscow: Nauka, 1966)
69. Zvietcovich F et al. *Biomed. Opt. Express* **10** 3699 (2019)
70. Kirby M A et al. *J. Biomed. Opt.* **22** 121720 (2017)
71. Zhang H et al. *Photonics* **8** 207 (2021)
72. Rippy J R et al. *IEEE Open J. Eng. Med. Biol.* **2** 179 (2021)
73. Han Z et al. *J. Biomed. Opt.* **20** 020501 (2015)
74. Zvietcovich F et al. *Nature Commun.* **10** 4895 (2019)
75. Snieder R, Wapenaar K *Phys. Today* **63** (9) 44 (2010)
76. Marmin A et al. *J. Biomed. Opt.* **26** 086006 (2021)
77. Larin K V, Sampson D D *Biomed. Opt. Express* **8** 1172 (2017)
78. Landau L D, Lifshitz E M *Theory of Elasticity* (Oxford: Pergamon Press, 1986); Translated from Russian: *Teoriya Uprugosti* (Moscow: Nauka, 1987)
79. Pan B et al. *Meas. Sci. Technol.* **20** 062001 (2009)
80. Rogowska J et al. *Heart* **90** 556 (2004)
81. Rogowska J et al. *British J. Radiology* **79** 707 (2006)
82. Fu J, Pierron F, Ruiz P *J. Biomed. Opt.* **18** 121512 (2013)
83. Nahas A et al. *Biomed. Opt. Express* **4** 2138 (2013)
84. Zaitsev V Y et al. *J. Biomed. Opt.* **20** 075006 (2015)
85. Fu J et al. *Exp. Mech.* **56** 1203 (2016)
86. Kurokawa K et al. *Opt. Lett.* **40** 2153 (2015)
87. Li E et al. *Opt. Lett.* **44** 787 (2019)
88. Meng F et al. *Appl. Sci.* **9** 1349 (2019)
89. Kennedy B F et al. *Biomed. Opt. Express* **3** 1865 (2012)
90. Zaitsev V Y et al. *Proc. SPIE* **9887** 98871G (2016)
91. Müller H H et al. *Biomed. Opt. Express* **3** 1025 (2012)
92. Bai Y et al. *Opt. Express* **29** 25327 (2021)
93. Li J et al. *Biomed. Opt. Express* **13** 2224 (2022)
94. Zaitsev V Y et al. *J. Biophoton.* **9** 499 (2016)
95. Zaitsev V Y et al. *J. Biomed. Opt.* **21** 116005 (2016)
96. Matveyev A L et al. *Laser Phys. Lett.* **15** 065603 (2018)
97. Zaitsev V Y et al. *Photonics* **8** 527 (2021)
98. Kling S, Khodadadi H, Goksel O *Front. Bioeng. Biotechnol.* **7** 453 (2020)
99. Kling S *J. R. Soc. Interface* **17** 20190786 (2020)
100. Singh M et al. *Photonics* **8** 111 (2021)
101. Sobol' E N et al. *Laser Phys.* **16** 735 (2006)
102. Bolshunov A et al. *Acta Ophthalmologica* **89** s248 (2011)
103. Sobol E N et al. *Laser Phys. Lett.* **4** 488 (2007)
104. Svistushkin V M et al. *Farmateka* **27** (5) 72 (2020)
105. Zaitsev V Y et al. *Laser Phys. Lett.* **13** 115603 (2016)
106. Zaitsev V Y et al. *J. Biophoton.* **10** 1450 (2017)
107. Zaitsev V Y et al. *J. Biophoton.* **12** e201800250 (2019)
108. Baum O I et al. *J. Biophoton.* **13** e201900199 (2020)
109. Baum O I et al. *Quantum Electron.* **50** 87 (2020); *Kvantovaya Elektron.* **50** 87 (2020)
110. Baum O I et al. *Laser Phys. Lett.* **16** 035603 (2019)
111. Alexandrovskaya Yu M et al. *Laser Phys. Lett.* **17** 085603 (2020)
112. Matveev L A et al. *SPIE Proc.* **11359** 113590G (2020)
113. Zaitsev V Y et al. *SPIE Proc.* **11242** 1124202 (2020)
114. Zaitsev V Y et al. *Laser Phys. Lett.* **16** 065601 (2019)
115. Lawman S et al. *Biomed. Opt. Express* **8** 5579 (2017)
116. Tuchin V V, Zhu D, Genina E A (Eds) *Handbook of Tissue Optical Clearing. New Prospects in Optical Imaging* (Boca Raton, FL: CRC Press, 2022) https://doi.org/10.1201/9781003025252
117. Genina E A et al. *J. Biomed. Photon. Eng.* **1** (1) 22 (2015)
118. Alexandrovskaya Y M et al., in *Handbook of Tissue Optical Clearing. New Prospects in Optical Imaging* (Eds V V Tuchin, D Zhu, E A Genina) (Boca Raton, FL: CRC Press, 2022) p. 185
119. Alexandrovskaya Y et al. *Materials* **15** 904 (2022)
120. Kennedy K M et al. *Sci. Rep.* **5** 15538 (2015)
121. Zaitsev V Y et al. *J. Innovative Opt. Health Sci.* **10** 1742006 (2017)
122. Zaitsev V Y et al. *J. Biophoton.* **14** e202000257 (2021)
123. Sovetsky A A et al. *Laser Phys. Lett.* **15** 085602 (2018)
124. Sovetsky A A et al. *Laser Phys. Lett.* **17** 065601 (2020)
125. Krouskop T A et al. *Ultrasonic Imaging* **20** (4) 260 (1998)
126. Plekhanov A A et al. *Sovremennye Tekhnol. Med.* **10** (3) 43 (2018)
127. Plekhanov A A et al. *Sci. Rep.* **10** 11781 (2020)
128. Sirotkina M A et al. *Biomed. Opt. Express* **11** 1365 (2020)
129. Kennedy B F et al. *Cancer Res.* **75** 3236 (2015)
130. Allen W M et al. *Biomed. Opt. Express* **7** 4139 (2016)
131. Chin L et al. *J. Biophotonics* **10** 690 (2017)
132. Kennedy K M et al. *Cancer Res.* **80** 1773 (2020)
133. Gubarkova E V et al. *Biomed. Opt. Express* **10** 2244 (2019)
134. Gubarkova E V et al. *Proc. SPIE* **11228** 112282F (2020)
135. Gubarkova E V et al. *Proc. SPIE* **11457** 1145709 (2020)
136. Sovetsky A A et al. *Proc. SPIE* **11359** 113590H (2020)
137. Gubarkova E V et al. *Proc. SPIE* **11952** 119520C (2022)
138. Gubarkova E V et al. *Diagnostics* **10** 994 (2020)
139. Gurbatov S N et al. *Acoust. Phys.* **55** 510 (2009); *Akust. Zh.* **55** 496 (2009)
140. Klemin V A et al. *Bull. Russ. Acad. Sci. Phys.* **82** 536 (2018); *Izv. Ross. Akad. Nauk. Fiz.* **82** 607 (2018)
141. Plekhanov A A et al. *SPIE Proc.* **11645** 11645X (2021)
142. Rudenko O V *Phys. Usp.* **49** 69 (2006); *Usp. Fiz. Nauk* **176** 77 (2006)
143. Zaitsev V Yu, Nazarov V E, Talanov V I *Phys. Usp.* **49** 89 (2006); *Usp. Fiz. Nauk* **176** 97 (2006)
144. Zaitsev V Y *MRS Bull.* **44** 350 (2019)
145. Morlier P *Rock Mech.* **3** 125 (1971)
146. Gubarkova E V et al. *Materials* **15** 3308 (2022)
147. Gubarkova E V et al. *Laser Phys. Lett.* **20** 065601 (2023)